Monthly Notices
of the
ROYAL ASTRONOMICAL SOCIETY

Mon. Not. R. Astron. Soc. **418,** 1285–1307 (2011) doi:10.1111/j.1365-2966.2011.19577.x

The effects of dust on the optical and infrared evolution of SN 2004et

J. Fabbri,[1] M. Otsuka,[2] M. J. Barlow,[1⋆] Joseph S. Gallagher,[3,4] R. Wesson,[1] B. E. K. Sugerman,[5] Geoffrey C. Clayton,[3] M. Meixner,[2] J. E. Andrews,[3] D. L. Welch[6] and B. Ercolano[7,8]

[1]*Department of Physics and Astronomy, University College London, Gower Street, London WC1E 6BT*
[2]*Space Telescope Science Institute, 3700 San Martin Drive, Baltimore, MD 21218, USA*
[3]*Department of Physics and Astronomy, Louisiana State University, Baton Rouge, LA 70803, USA*
[4]*Department of Mathematics, Physics, and Computer Science, Raymond Walters College, University of Cincinnati, 9555 Plainfield Road, Blue Ash, OH 45236, USA*
[5]*Department of Physics and Astronomy, Goucher College, 1021 Dulaney Valley Road, Baltimore, MD 21204, USA*
[6]*Department of Physics and Astronomy, McMaster University, Hamilton, ON L8S 4M1, Canada*
[7]*Universitäts-Sternwarte München, Scheinerstr. 1, 81679 München, Germany*
[8]*Cluster of Excellence 'Origin and Structure of the Universe', Boltzmannstr. 2, 85748 Garching, Germany*

Accepted 2011 August 3. Received 2011 June 27; in original form 2011 May 6

ABSTRACT

We present an analysis of multi-epoch observations of the Type II-P supernova SN 2004et. New and archival optical spectra of SN 2004et are used to study the evolution of the Hα and [O I] 6300-Å line profiles between days 259 and 646. Mid-infrared imaging with Michelle on Gemini-North and with all three instruments of the *Spitzer Space Telescope* was carried out between 2004 and 2010, supplemented by archival *Spitzer* data. We include *Spitzer* 'warm' mission photometry at 3.6 and 4.5 μm obtained on days 1779, 1931 and 2151, along with ground-based and *Hubble Space Telescope* (*HST*) optical and near-infrared observations obtained between days 79 and 1803. Multiwavelength light curves are presented, as well as optical–infrared spectral energy distributions (SEDs) for multiple epochs. Starting from about day 300, the optical light curves provide evidence for an increasing amount of circumstellar extinction attributable to newly formed dust, with the additional extinction reaching 0.8–1.5 mag in the V band by day 690. The overall SEDs were fitted with multiple blackbody components, in order to investigate the luminosity evolution of the supernova, and then with Monte Carlo radiative transfer models using smooth or clumpy dust distributions, in order to estimate how much new dust condensed in the ejecta. The luminosity evolution was consistent with the decay of ^{56}Co in the ejecta up until about day 690, after which an additional emission source is required, in agreement with the findings of Kotak et al. Clumped dust density distributions consisting of 20 per cent amorphous carbons and 80 per cent silicates by mass were able to match the observed optical and infrared SEDs, with dust masses that increased from $8 \times 10^{-5}\,M_\odot$ on day 300 to $1.5 \times 10^{-3}\,M_\odot$ on day 690, still significantly lower than the values needed for core-collapse supernovae to make a significant contribution to the dust enrichment of galaxies.

Key words: circumstellar matter – supernovae: individual: SN 2004et.

1 INTRODUCTION

Theoretical studies by Kozasa, Hasegawa & Nomoto (1989), Todini & Ferrara (2001), Nozawa et al. (2003) and Bianchi & Schneider (2007) of dust formation in the ejecta of core-collapse supernovae (CCSNe) produced by massive stars suggested that they could each produce up to 0.1–1.0 $M_\odot$ of dust and thereby act as major sources of dust in galaxies. The discovery at submillimetre wavelengths of large quantities of dust in very young high-redshift galaxies (e.g. Bertoldi et al. 2003; Maiolino et al. 2004; Dwek, Galliano & Jones 2007) seemed to reinforce the case for massive star CCSNe as major dust contributors. However, studies at infrared (IR) wavelengths of Type II CCSNe in the nearby Universe have to date not confirmed these dust production predictions. SN 1987A in the Large Magellanic Cloud condensed less than $10^{-3}\,M_\odot$ of dust in its ejecta

⋆E-mail: mjb@star.ucl.ac.uk

(Wooden et al. 1993; Ercolano, Barlow & Sugerman 2007), while SN 2003gd in M74 produced less than a few $\times 10^{-3}\,M_{\odot}$ of new dust by day 499 (Sugerman et al. 2006; Meikle et al. 2007). For a number of other recent Type II CCSNe, estimates for the quantities of new dust formed in their ejecta have not exceeded $10^{-3}\,M_{\odot}$ (Andrews et al. 2010, 2011; Meikle et al. 2011; Szalai et al. 2011).

Kotak et al. (2009) studied the multiwavelength evolution of the Type II-P SN 2004et, the eighth SN to be discovered in the past century in the nearby spiral galaxy NGC 6946. We report here our own multiwavelength observations and analysis of the dust production by this SN. Following Li et al. (2005), we adopt an explosion date of 2004 September 22 (JD 245 3270.5) as the day 0 epoch to which our observation dates are referenced. Section 2 provides a brief overview of previously published optical and IR observations of SN 2004et. Section 3 describes the Hα and [O I] 6300-Å line profiles obtained from a sequence of optical spectra of SN 2004et, while Section 4 describes our mid-IR observations. The resulting mid-IR fluxes are presented in Section 4.2, together with a discussion of the mid-IR light-curve evolution. Complementary photometric data, obtained by us at optical and near-IR (NIR) wavelengths using the *Hubble Space Telescope* (*HST*) and Gemini-North telescopes, are presented in Section 5. The spectral energy distributions (SEDs) of SN 2004et at different epochs are discussed in Section 6. This section includes blackbody fitting to the SEDs, allowing limits to be placed on the physical properties of the SN at the various epochs. Using Monte Carlo radiative transfer (RT) models, we estimate ejecta dust masses in Section 7. Finally, the results from our multi-epoch analysis of SN 2004et are summarized in Section 8, along with the implications for dust production by Type II SNe.

2 PREVIOUS STUDIES OF SN 2004et

2.1 Optical observations

Zwitter, Munari & Moretti (2004) reported that an echelle spectrum taken on 2004 September 28 showed a relatively featureless spectrum with very broad, low-contrast Hα emission, suggesting SN 2004et to be a Type II event. This was confirmed by a low-resolution spectrum taken on 2004 October 1 (Filippenko et al. 2004), which showed the P Cygni profile of Hα to be dominated by the emission component, but that the other hydrogen Balmer lines had more typical P Cygni profiles. The continuum was reported as quite blue but dropping off steeply shortwards of 4000 Å.

The V-, R- and I-band light curves showed SN 2004et to be a Type II-P (plateau) SN (Li et al. 2005), but it exhibited some differences when compared with the typical Type II-P SN 1999em. Evolution was slower in the U and B bands, consistent with the $(U - B)$ and $(B - V)$ colour evolution, leading Li et al. (2005) to conclude that SN 2004et seemed to evolve more slowly than SN 1999em, especially in the violet part of the spectrum.

Extensive photometric and spectroscopic monitoring in the optical was carried out by Sahu et al. (2006) from days 8 to 541 after explosion. They confirmed the SN to be of Type II-P based on the plateau observed in the *VRI* bands which lasted for ∼110 d after the explosion. From their light-curve analysis, they determined that the SN was caught at a very early stage soon after the shock breakout, reaching a maximum B-band magnitude ∼10 d after explosion. They also found that the decline rate of the light curve during the early nebular phase (∼180–310 d) was similar to the radioactive decay rate of ^{56}Co, indicating that γ-ray trapping was efficient during this time, and estimated that $0.06 \pm 0.02\,M_{\odot}$ of ^{56}Ni was synthesized during the explosion of SN 2004et, in agreement with the subsequent estimates of Misra et al. (2007) and Maguire et al. (2010). Based on the plateau luminosity and duration and the mid-plateau expansion velocity, Sahu et al. (2006), Misra et al. (2007) and Maguire et al. (2010) have estimated explosion energies for SN 2004et in the range $(0.88–1.20) \times 10^{51}$ erg.

2.2 Distance and reddening

There are many estimates in the literature for the distance to the host galaxy NGC 6946. Sahu et al. (2006) summarized a few of these and included the result from their own analysis of SN 2004et using the standard candle method of Nugent et al. (2006) for Type II-P SNe, deriving an average distance of 5.6 Mpc. Herrmann et al. (2008) estimated a distance of 6.1 ± 0.6 Mpc to NGC 6946 using the planetary nebula luminosity function. For consistency with our previous studies of SN 2002hh (Barlow et al. 2005; Welch et al. 2007) and SN 2008S (Wesson et al. 2010), we adopt the distance of 5.9 ± 0.4 Mpc to NGC 6946 estimated by Karachentsev, Sharina & Huchtmeier (2000) from the brightest stars method.

From Schlegel, Finkbeiner & Davis (1998), the foreground Galactic reddening towards SN 2004et is estimated to be $E(B - V) = 0.34$ mag. Zwitter et al. (2004) used the equivalent width of Na I D 2 lines from their high-resolution echelle spectra to estimate a total reddening (Galactic + host) towards the SN of $E(B - V) = 0.41$ mag. Sahu et al. (2006) used similar analysis with their lower resolution spectra to obtain a comparable value of $E(B - V) = 0.43$ mag. We adopt a total reddening to SN 2004et of $E(B - V) = 0.41$ mag.

2.3 Evidence for dust production by SN 2004et

From their spectroscopic observations of the temporal evolution of the Hα and [O I] 6300-, 6363-Å line profiles from days 277 to 465, Sahu et al. (2006) noted a blueshifting after day 300 of the emission peak of both features and a flattening of the Hα emission peak. This, together with a steepening of the light curve after day ∼320, they interpreted as indications of early dust formation in the ejecta of SN 2004et. Misra et al. (2007) also found that the rate of decline in the optical light curves accelerated between ∼320 and 386 d.

Fabbri, Sugerman & Barlow (2005) reported the day 64 detection of SN 2004et in all the four *Spitzer* Infrared Array Camera (IRAC) bands, from 3.6 to 8.0 μm, in Spitzer Infrared Nearby Galaxies Survey (SINGS) Legacy programme archival images of NGC 6946 (see Section 4.1). Kotak et al. (2009) presented archival and their own *Spitzer* mid-IR observations of SN 2004et obtained up to day 1406, together with late-time optical spectra. They concluded that between days 300 and 795, the SED was comprised of three components – hot, warm and cold – each, respectively, due to emission from optically thick gas, newly formed, ejecta-condensed dust and an IR echo from the interstellar medium of the host galaxy. They estimated that the mass of dust formed in the ejecta grew to a few $\times 10^{-4}\,M_{\odot}$, located in comoving clumps of fixed size. From their *Spitzer* Infrared Spectrometer (IRS) spectra, they reported the first spectroscopic evidence of silicate dust formed in the ejecta of a SN, supported by the detection of strong but declining molecular SiO emission in the 8-μm region. They interpreted the appearance of broad, box-shaped optical emission-line profiles about 2 year post-explosion as due to the impact of the ejecta on the circumstellar medium (CSM) of the progenitor star, resulting in the formation of a cool, dense shell to which they attributed responsibility for a later rise in the mid-IR emission from SN 2004et.

Table 1. Log of optical spectroscopic observations of SN 2004et from the SEEDS collaboration (GMOS-N, PI: Clayton), from Sahu et al. (2006) and from online archives (TNG and Subaru).

Date	Age (d)	Telescope/ instrument	Wavelength range (Å)	Exp. time (s)	Program ID	Principal investigator
2005-06-07	259	HCT HFOSC[a]	3500–7000; 5200–9200	1 × 900	–	Sahu et al. (2006)
2005-08-01	314	HCT HFOSC[a]	3500–7000; 5200–9200	1 × 900	–	Sahu et al. (2006)
2005-08-05	317	Gemini GMOS-N	3500–10 000	3 × 900	GN-2005B-Q-54	G. Clayton
2005-08-29	336	TNG LRS[b]	3890–8000	1 × 1800	AOT12 CAT-G109	E. de la Rosa
2005-10-17	391	HCT HFOSC[a]	3500–7000; 5200–9200	1 × 900	–	Sahu et al. (2006)
2005-10-31	404	Gemini GMOS-N	3500–10 000	3 × 900	GN-2005B-Q-54	G. Clayton
2005-11-23	428	HCT HFOSC[a]	3500–7000; 5200–9200	1 × 900	–	Sahu et al. (2006)
2006-06-30	646	Subaru FOCAS[c]	4670–8970	2 × 900	S06A-152	K. Kawabata

[a] Raw data, including calibration frames and flux standards, provided by Sahu et al. (2006).
[b] Raw and calibration data were downloaded from the online TNG archive at http://ia2.oats.inaf.it/.
[c] Raw and calibration data downloaded from the online Subaru Mitaka Okayama Kiso Archive (SMOKA) at http://smoka.nao.ac.jp/index.jsp.

Maguire et al. (2010) reported optical and NIR photometric and spectroscopic observations of SN 2004et carried out from just after explosion to +500 d. Their NIR spectrum at day 306 showed a clear detection of the first overtone band of CO at ∼2.3 μm, which they interpreted as being a signature of dust formation. By analysing the optical light curves in the early nebular phase, they found that the *BVR* decline rates between days ∼136 and 296 were consistent with those expected from light curves powered by the radioactive decay of ^{56}Co (assuming complete γ-ray trapping). However, between days ∼296 and 414 they found that these decline rates had steepened. They also noted a significant blueshift in the peak of the Hα emission line from days ∼300 to 464, in agreement with the results of Sahu et al. (2006). These results were interpreted as signatures of dust formation occurring post 300 d. Their very late time (>1000 d) photometry showed a flattening of the optical and NIR light curves, which they mainly attributed to the interaction of the SN ejecta with the CSM, following the work of Kotak et al. (2009).

3 OPTICAL SPECTROSCOPY OF SN 2004et

As part of the Survey for Evolution of Emission from Dust in Supernovae (SEEDS) programme, Gemini-North spectroscopic observations of SN 2004et were obtained on 2005 August 5 and October 31, corresponding to 317 and 404 d after explosion. A log of these and the other Hα-region observations that we analyse here can be found in Table 1. We utilized the Gemini Multi-Object Spectrograph on Gemini-North (GMOS-N) equipped with a 0.75-arcsec slit width and the B600-G5303 grating in long-slit mode with a position angle of 296°. Three spectra were obtained during each epoch with identical exposure times of 900 s. The central wavelengths of the images were 5950, 5970 and 5990 Å, respectively, to allow for gap removal of the combined spectra. A 2 × 2 binning of the CCD pixels in the low gain setting was employed. All spectra were taken with adjacent GMOS baseline calibration flat exposures to correct for sensitivity gradients across the CCD, and CuAr spectra were utilized for the initial calibration of the dispersion solution.

Our GMOS-N spectra were reduced using the Gemini IRAF package. Pipeline-processed calibration images were obtained from the Gemini Science Archive. The spectra were trimmed and then overscan-, bias- and flat-field-corrected using the task `gsreduce`. Wavelength calibration solutions were determined from the CuAr lamp spectra using `gswavelength`, and the solution was applied to the SN 2004et spectra via `gstransform`. Object spectra were extracted using `gsextract`. The observations were not flux calibrated since our primary goal was to monitor the evolution of the line profiles.

Sahu et al. (2006) presented photometric and spectroscopic data for SN 2004et from approximately 8 to 541 d after the explosion. Their results showed a shift to the blue of the central peak of both Hα and [O I] 6300, 6363 Å at late times. They concluded that this was indicative of new dust formed in the ejecta of SN 2004et. However, comparisons between the Hα profiles in our GMOS-N spectra and those at similar epochs in the archived calibrated spectra of Sahu et al. (2006), obtained from the Online Supernova Spectrum Archive (SUSPECT),[1] showed some inconsistencies, with their spectra showing clear blueshifting of the Hα emission-line profile between days 314 and 391, while our own spectra showed little change between days 317 and 404. In order to help resolve this discrepancy, Sahu et al. (2006) generously provided their raw data for SN 2004et for several of the epochs presented in their paper. This allowed us to reduce the respective sets of data in the same way. A description of the observational set-up used by Sahu et al. (2006) can be found in their paper.

We also obtained two archival spectroscopic observations of SN 2004et, taken on days 336 and 646. The earlier epoch corresponds to an observation on 2005 August 29 taken with the low-resolution spectrograph on the 3.58-m Telecopio Nazionale Galileo (TNG) on La Palma. The latter epoch corresponded to an observation on 2006 June 30 with the Faint Object Camera and Spectrograph (FOCAS) on the 8.2-m Subaru Telescope on Mauna Kea in Hawaii. The reduction procedure matched that carried out by us for the GMOS-N and Sahu et al. (2006) spectra.

Since our goal was to self-consistently align a number of spectra taken with four different instrument/telescope set-ups, we did not rely solely on the initial wavelength calibrations. During the extraction of each SN spectrum, a sky spectrum was also extracted that was ultimately subtracted from the SN spectrum. Since the sky and SN spectra possessed identical wavelength calibrations, we derived corrections to the initial wavelength calibrations of each of the SN spectra using the strong and narrow [O I] 5577- and 6300-Å sky emission lines.

The temporal evolution of the Hα profile between days 259 and 646, following our re-analysis of the combined set of spectra, is depicted in the left-hand panel of Fig. 1. The spectra are displayed

[1] http://bruford.nhn.ou.edu/~suspect; Richardson et al. (2001).

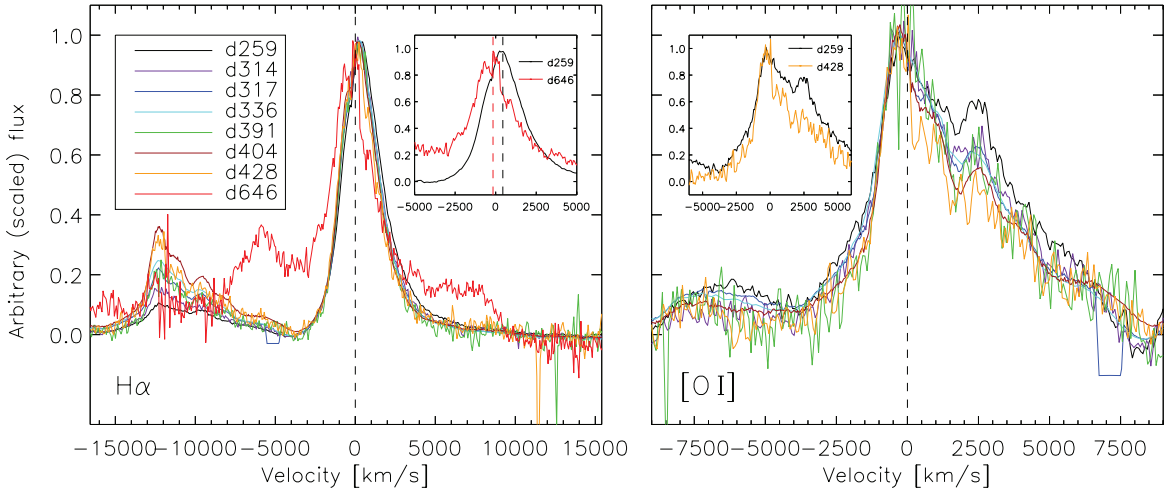

Figure 1. The Hα and [O I] profile evolution. The left-hand panel shows the Hα spectra from days 259 to 646, with the normalized continua subtracted to a zero-level and the peaks of the emission line normalized to unity. The dashed vertical line in the main plot corresponds to the rest wavelength of Hα (NGC 6946 has a radial velocity of $+40\,\mathrm{km\,s^{-1}}$). The inset shows a comparison of the earliest and latest Hα spectra, obtained just over a year apart, to highlight the blueshifting ($\sim$600 km s^{-1}) during this interval. The dashed lines in the inset plot indicate the measured line centres. The right-hand panel shows the evolution of the [O I] 6300-Å profile from days 259 to 428. The dashed line in the main plot indicates the rest velocity of the 6300-Å line. The emission feature in the red wing corresponds to the [O I] 6363-Å line. The spectra from days 259, 314, 391 and 428 are from Sahu et al. (2006; raw data kindly provided by the authors and calibrated by us). The spectra from days 317 and 404 are SEEDS GMOS-N observations, and those from days 336 and 646 are from archival TNG-Low Resolution Spectrograph (LRS) and Subaru-FOCAS spectra, respectively.

in velocity space, with the continua subtracted and the peaks of the emission line normalized to approximately unity. The inset shows a close-up view of the earliest and latest Hα profiles, obtained just over a year apart at days 259 and 646, to highlight the overall blueshifting of the profile during this time. The dashed lines in the inset indicate the line peak centres measured on days 259 and 646, with the blueshifting of the latter profile providing strong evidence for the formation of dust in the ejecta during the intervening period, as described by Lucy et al. (1989) for SN 1987A.

The Hα line profiles presented by Sahu et al. (2006) showed a significant blueshifting with time of the emission peak, amounting to a few hundred km s^{-1}, with the largest shift appearing to occur between days 277 and 314. Sahu et al. (2006) did not quantify the shifts in their Hα profiles, beyond stating that a blueshift in the emission peak was clearly seen after day 300 in their day 277–465 Hα (and [O I] 6300, 6363 Å) profiles. Kotak et al. (2009) confirmed this from their own analysis of the Sahu et al. (2006) spectra, reporting a shift of $-400\,\mathrm{km\,s^{-1}}$ in the whole Hα profile between days 301 and 314, but little sign of a progressive blueshifting during the subsequent day 314–465 period. Using the Sahu et al. (2006) spectra, along with additional spectra, Maguire et al. (2010) found that the peak of the Hα emission line was at $+280 \pm 50\,\mathrm{km\,s^{-1}}$ between days 163 and 300, but from days 314 to 464 showed a constant blueshift, to $-137\,\mathrm{km\,s^{-1}}$.

We have used our recalibrated spectral data set to measure the wavelength of peak Hα emission in each of the profiles plotted in Fig. 1. The evolution of the peak wavelength is shown in Fig. 2. The line peaks show an overall blueshifting between days 259 and 646 of $\sim$13.2 Å, corresponding to a velocity shift of $\sim -600\,\mathrm{km\,s^{-1}}$. Between days 259 and 314, we measure an initial blueshift of $\sim$3 Å ($\approx$140 km s^{-1}), not as large as the 400 km s^{-1} shift between days 301 and 314 measured by Kotak et al. (2009) from the Sahu et al. (2006) spectra in the SUSPECT archive. While we find little change between days 314/317 and day 391 in the measured emission-line peaks in the recalibrated spectral data set (Fig. 2), between days 404 and 428 we measure a blueshifting of the emission peak by

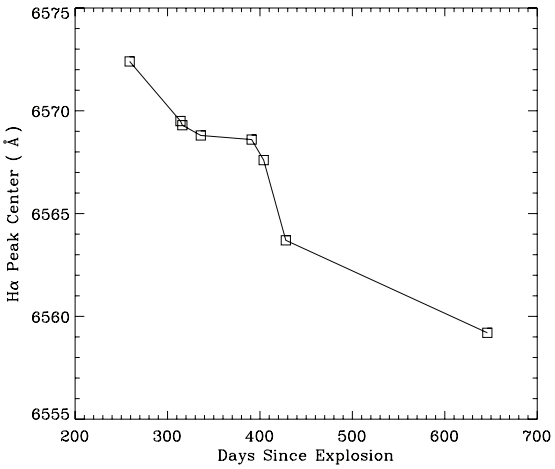

Figure 2. The evolution with time of the measured wavelength of the Hα emission peak of SN 2004et.

$\sim$4 Å (185 km s^{-1}) followed by a further blueshifting of $\sim$4.5 Å (205 km s^{-1}) between the spectra obtained at days 428 and 646. We therefore find that the majority of the blueshifting occurred after day 391.

Whilst there is no strong evidence for a developing line asymmetry in the earlier epoch Hα profiles (Fig. 1), a diminution of the red wing can be discerned by days 428 and 646. By day 646, a significant blueshifting ($\sim$4.5 Å) of the whole profile since day 428 is evident, with multiple peaks evident at the centre of the profile, although there are earlier inflections in the blue wing of the Hα profiles. Two broad features either side of the main emission line (at $\sim +7000$ and $-6000\,\mathrm{km\,s^{-1}}$) have appeared by day 646. Kotak et al. (2009) presented three later optical spectra of SN 2004et, obtained with the Keck telescopes on days 823, 933 and 1146, which show similarities to, and a development of, the Subaru day 646 Hα profile. They described the Hα profile from the late-time Keck spectra as

having a steep-sided, box-like component, with a half-width at zero intensity (HWZI) of 8500 km s^{-1} and noted that the characteristic ejecta profile of Hα seen in the Sahu et al. (2006) spectra may still be present at days 823 and 933, with a HWZI of $\sim$2000 km s^{-1}, but that its presence at day 1146 was less certain.

The 6300- and 6363-Å lines of [O I] can be seen in emission on the blue side of the Hα profiles plotted in Fig. 1. In the right-hand panel of Fig. 1, we have plotted the [O I] 6300-Å velocity profiles for days 259 through to 428 (the day 646 profile had too low a signal-to-noise ratio). The inset compares the day 259 and day 428 [O I] profiles, showing a clear diminution of the red wing of the day 428 profile relative to day 259.

4 MID-INFRARED OBSERVATIONS

4.1 Gemini-Michelle and *Spitzer* photometry

NGC 6946, the host galaxy of SN 2004et, was observed with *Spitzer* by the SINGS Legacy programme (Kennicutt et al. 2003) between 2004 June and November, such that the region of the SN was serendipitously imaged pre- and post-explosion. Fig. 3 shows the position of the SN in relation to its host galaxy NGC 6946 in the pre- and post-explosion SINGS IRAC images, together with a closer view of the SN region in the different IRAC wavebands.

SN 2004et was clearly detected in the SINGS IRAC image at day 64 and was subsequently monitored with IRAC, Multiband-Imaging Photometer for Spitzer (MIPS) and the IRS peak-up imaging (PUI) module via our *Spitzer* GO programmes during Cycles 2, 3, 4, 6 and 7 (Cycle 6 was the beginning of the *Spitzer* 'warm' mission, in which the observatory operates using only the 3.6- and 4.5-μm IRAC channels). Archival *Spitzer* data for the SN from Cycles 2 and 3 were also downloaded to provide a more complete time sample of the SN's mid-IR evolution. In summary, post-explosion mid-IR observations of SN 2004et were taken between 2004 November and 2010 August, corresponding to an age range of 64–2151 d. With the *Spitzer Space Telescope*, there are 12 epochs of observations in each of the four IRAC wavebands, with a further three epochs of IRAC observations during the 'warm' mission in just the 3.6- and 4.5-μm channels. There are eight epochs of IRS-PUI observations at 16 μm and nine epochs of MIPS 24-μm observations. Of the 33 individual *Spitzer* observations listed in Table 2, the first three were obtained by the SINGS Legacy programme, five were obtained by programmes led by PIs Meikle and Kotak, and 25 were obtained by our SEEDS programme.

In addition to the *Spitzer* mid-IR observations, broad-band N′ photometry at 11.2 μm was obtained with Michelle on Gemini-North during 2005, 2006, 2007 and 2008, consisting of six observations at the four epochs. A time-ordered list of all the *Spitzer* and Michelle mid-IR observations of SN 2004et is provided in Table 2. The listed exposure time is the total time spent on-source. The final column provides a key to the list of observing programmes from which these data were obtained; the programme number and principal investigator are detailed in a footnote to the table. Data retrieved from the archive are marked as such. Appendix A1 describes how the mid-IR data were processed.

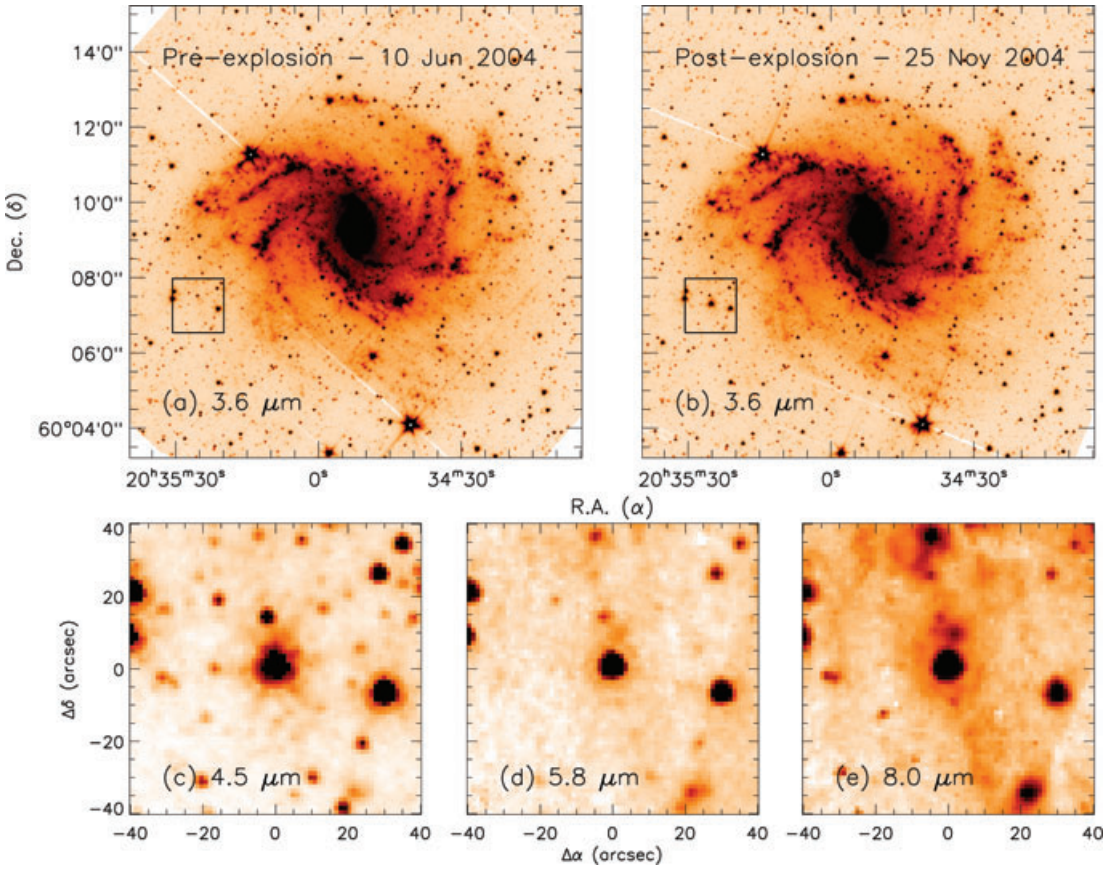

Figure 3. The position of SN 2004et in SINGS Legacy IRAC images of NGC 6946. Panels (a) and (b) show the whole galaxy at 3.6-μm pre- (day −104) and post-explosion (day 64), respectively. The square is centred on the SN coordinates, with the SN clearly evident at day 64. Panels (c), (d) and (e) zoom in on the square region of the SN field at 4.5, 5.8 and 8.0 μm, respectively, at day 64.

Table 2. Summary of the mid-IR imaging observations of SN 2004et with the *Spitzer Space Telescope* and Gemini-North.

UT date	Age (d)	Detector	$\lambda_{\rm eff}$ (μm)	Field of View (FoV) (arcmin^2)	Pixel scale (arcsec pixel^{-1})	Exp. time (s)	Ref.
2004-06-10	−104	IRAC	3.6/4.5/5.8/8.0	5.2 × 5.2	1.2	107.2	1
2004-07-09	−75	MIPS	24.0	5.4 × 5.4	1.5	161.5	1
2004-11-25	64	IRAC	3.6/4.5/5.8/8.0	5.2 × 5.2	1.2	107.2	1
2005-07-13	294	IRS-PUI	16.0	1.0 × 1.2	1.2	629.2	2
2005-07-19	300	IRAC	3.6/4.5/5.8/8.0	5.2 × 5.2	0.75	14.4	3
2005-07-30	311	Michelle	11.2 (N′)	0.5 × 0.4	0.1	1081.9	4
2005-08-03	315	MIPS	24.0	5.4 × 5.4	0.75	140.0	3
2005-09-17	360	IRAC	3.6/4.5/5.8/8.0	5.2 × 5.2	0.75	14.4	3
2005-09-24	367	MIPS	24.0	5.4 × 5.4	0.75	140.0	3
2005-11-02	406	IRAC	3.6/4.5/5.8/8.0	5.2 × 5.2	0.75	536.0	2
2005-12-22	456	IRS-PUI	16.0	1.0 × 1.2	1.2	629.2	2
2005-12-30	464	IRAC	3.6/4.5/5.8/8.0	5.2 × 5.2	0.75	14.4	3
2006-01-11	476	MIPS	24.0	5.4 × 5.4	0.75	140.0	3
2006-05-12	597	Michelle	11.2 (N′)	0.5 × 0.4	0.1	811.4	5
2006-05-14	599	Michelle	11.2 (N′)	0.5 × 0.4	0.1	376.3	5
2006-08-04	681	IRS-PUI	16.0	1.0 × 1.2	1.2	629.2	6
2006-08-13	690	IRAC	3.6/4.5/5.8/8.0	5.2 × 5.2	0.75	14.4	7
2006-09-01	709	MIPS	24.0	5.4 × 5.4	0.75	140.0	7
2006-09-10	718	IRS-PUI	16.0	1.0 × 1.2	1.2	56.6	7
2006-12-29	828	IRAC	3.6/4.5/5.8/8.0	5.2 × 5.2	0.75	124.8	7
2007-01-21	851	MIPS	24.0	5.4 × 5.4	0.75	420.0	7
2007-01-27	857	IRS-PUI	16.0	1.0 × 1.2	1.2	132.1	7
2007-06-26	1007	IRS-PUI	16.0	1.0 × 1.2	1.2	283.1	7
2007-07-03	1015	IRAC	3.6/4.5/5.8/8.0	5.2 × 5.2	0.75	321.6	7
2007-07-09	1020	Michelle	11.2 (N′)	0.5 × 0.4	0.1	1999.2	8
2007-07-10	1021	MIPS	24.0	5.4 × 5.4	0.75	420.0	7
2007-08-02	1044	IRS-PUI	16.0	1.0 × 1.2	1.2	283.1	9
2007-08-12	1054	IRAC	3.6/4.5/5.8/8.0	5.2 × 5.2	0.75	321.6	9
2007-08-27	1069	MIPS	24.0	5.4 × 5.4	0.75	420.0	9
2007-12-09	1173	IRS-PUI	16.0	1.0 × 1.2	1.2	283.1	9
2007-12-27	1191	IRAC	3.6/4.5/5.8/8.0	5.2 × 5.2	0.75	321.6	9
2008-01-07	1202	MIPS	24.0	5.4 × 5.4	0.75	420.0	9
2008-01-17	1212	IRS-PUI	16.0	1.0 × 1.2	1.2	1258.4	10
2008-06-21	1368	Michelle	11.2 (N′)	0.5 × 0.4	0.1	1928.6	11
2008-07-09	1386	Michelle	11.2 (N′)	0.5 × 0.4	0.1	2257.9	12
2008-07-18	1395	IRAC	3.6/4.5/5.8/8.0	5.2 × 5.2	0.75	321.6	9
2008-07-29	1406	MIPS	24.0	5.4 × 5.4	0.75	420.0	9
2009-08-06	1779	IRAC	3.6/4.5	5.2 × 5.2	0.75	1161.6	13
2010-01-05	1931	IRAC	3.6/4.5	5.2 × 5.2	0.75	1161.6	13
2010-08-13	2151	IRAC	3.6/4.5	5.2 × 5.2	0.75	1161.6	14

(1) *Spitzer* Cycle 1 SINGS Legacy programme 00159, PI: Kennicutt. (2) Archival data, *Spitzer* Cycle 2 GO programme 20256, PI: Meikle. (3) This paper, *Spitzer* Cycle 2 GO programme 20320, PI: Sugerman. (4) This paper, Gemini semester 05A programme GN-2005A-Q-20, PI: Barlow. (5) This paper, Gemini semester 06A programme GN-2006A-Q-1, PI: Barlow. (6) Archival data, *Spitzer* Cycle 3 GO programme 30292, PI: Meikle. (7) This paper, *Spitzer* Cycle 3 GO programme 30494, PI: Sugerman. (8) This paper, Gemini semester 07A programme GN-2007A-Q-5, PI: Barlow. (9) This paper, *Spitzer* Cycle 4 GO programme 40010, PI: Meixner. (10) Archival data, *Spitzer* Cycle 4 GO programme 40619, PI: Kotak. (11) This paper, Gemini semester 07B programme GN-2007B-Q-4, PI: Barlow. (12) This paper, Gemini semester 08B programme GN-2008B-Q-44, PI: Barlow. (13) This paper, *Spitzer* Cycle 6 GO programme 60071, PI: Andrews. Cycle 6 took place during the *Spitzer* 'warm' mission following completion of the cryogenic mission. Only IRAC 3.6- and 4.5-μm channels were available, with expected sensitivity unchanged from performance in the cryogenic mission. (14) This paper, *Spitzer* Cycle 7 GO programme 70008, PI: Andrews, *Spitzer* 'warm' mission.

4.2 Evolution of the mid-IR emission

Table 3 lists the complete set of *Spitzer* and Gemini mid-IR flux densities and associated uncertainties/upper limits of SN 2004et from days 64 to 2151 as determined from the point spread function (PSF) fitting techniques described by Fabbri (2011). *Spitzer* IRAC, MIPS and IRS-PUI data have had pre-explosion flux levels subtracted. Measured (IRAC and MIPS) and estimated (PUI) pre-explosion flux densities at the position of the SN are summarized in the last row of the table.

The IRAC, PUI 16-μm and MIPS 24-μm light curves (with pre-explosion levels subtracted) are shown in Fig. 4. For clarity, the different light curves have been arbitrarily shifted by the factors shown. Upper limits to the flux densities at 3.6 and 5.8 μm are

Table 3. Mid-IR photometry of SN 2004et. The shaded rows indicate those fluxes across different wavebands considered as the same epoch.

UT date	Age (d)	Flux density[a]/upper limits[b] (μJy)						
		IRAC[c]				Michelle N′	IRS-PUI[c]	MIPS[c]
		3.6 μm	4.5 μm	5.8 μm	8.0 μm	11.2 μm	16 μm	24 μm
2004-06-10	−104	83.8 ± 10.2	45.4 ± 8.3	178 ± 25	412 ± 51	–	–	–
2004-07-09	−75	–	–	–	–	–	–	376 ± 25
2004-11-25	64	17 490 ± 532	13 038 ± 745	10 046 ± 179	6020 ± 91	–	–	–
2005-07-13	294	–	–	–	–	–	930 ± 33	–
2005-07-19	300	726 ± 61	3151 ± 97	1291 ± 218	2162 ± 154	–	–	–
2005-07-30	311	–	–	–	–	1700 ± 200	–	–
2005-08-03	315	–	–	–	–	–	–	832 ± 75
2005-09-17	360	430 ± 71	1728 ± 88	935 ± 285	1731 ± 156	–	–	–
2005-09-24	367	–	–	–	–	–	735 ± 74	
2005-11-02	406	315 ± 21	1045 ± 21	707 ± 79	1500 ± 77	–	–	–
2005-12-22	456	–	–	–	–	–	890 ± 32	–
2005-12-30	464	174 ± 67	656 ± 77	606 ± 293	952 ± 162	–	–	–
2006-01-11	476	–	–	–	–	–	–	686 ± 89
2006-05-12/14	597/599	–	–	–	–	≤650	–	–
2006-08-04	681	–	–	–	–	–	670 ± 34	–
2006-08-13	690	≤49	45.9 ± 15.3	115 ± 38	342 ± 114	–	–	–
2006-09-01	709	–	–	–	–	–	–	663 ± 77
2006-09-10	718	–	–	–	–	–	562 ± 30	–
2006-12-29	828	≤45	29.4 ± 9.8	≤87	145 ± 48	–	–	–
2007-01-21	851	–	–	–	–	–	–	513 ± 54
2007-01-27	857	–	–	–	–	–	446 ± 31	–
2007-06-26	1007	–	–	–	–	–	324 ± 29	–
2007-07-03	1015	≤23	14.1 ± 4.7	≤83	113 ± 37	–	–	–
2007-07-09	1020	–	–	–	–	≤400	–	–
2007-07-10	1021	–	–	–	–	–	–	644 ± 48
2007-08-02	1044	–	–	–	–	–	366 ± 35	–
2007-08-12	1054	≤34	15.1 ± 5.0	≤78	115 ± 38	–	–	–
2007-08-27	1069	–	–	–	–	–	–	610 ± 49
2007-12-09	1173	–	–	–	–	–	1023 ± 33	–
2007-12-27	1191	52.5 ± 17.5	189 ± 10	345 ± 75	458 ± 73	–	–	–
2008-01-07	1202	–	–	–	–	–	–	1276 ± 42
2008-01-17	1212	–	–	–	–	–	1055 ± 31	–
2008-06-21	1368	–	–	–	–	1036 ± 212	–	–
2008-07-09	1386	–	–	–	–	1016 ± 224	–	–
2008-07-18	1395	76.3 ± 22.6	258 ± 11	465 ± 49	578 ± 82	–	–	–
2008-07-29	1406	–	–	–	–	–	–	1563 ± 54
2009-08-06[d]	1779	17.3 ± 7.6	113 ± 8	–	–	–	–	–
2010-01-05[d]	1931	14.4 ± 6.9	90.3 ± 16.8	–	–	–	–	–
2010-08-13[d]	2151	7.2 ± 3.0	76.7 ± 5.3	–	–	–	–	–
Pre-explosion	83.8 ± 10.2	45.4 ± 8.3	178 ± 25	412 ± 51	–	221 ± 22		376 ± 25

[a] All post-explosion flux densities were measured with PSF-fitted photometry (using IRAF DAOPHOT). Pre-explosion IRAC and MIPS fluxes were measured in an aperture of radius 5 arcsec with sky annuli at inner radius 75 arcsec and outer radius 10 arcsec, respectively, using a 2σ clipped-mean sky algorithm (using IRAF `phot`).

[b] Flux upper limits for the non-detections in the Gemini-Michelle data are 3σ values based on the standard deviation of the background in the region of the SN position scaled to a diffraction-limited size aperture.

[c] *Spitzer* IRAC, MIPS and IRS-PUI data have had pre-explosion flux levels subtracted: IRAC and MIPS by use of difference imaging techniques to subtract pre-explosion SINGS images, and IRS-PUI by estimating the pre-explosion level from blackbody fits to the SED at day 1015 (see text). Measured (IRAC and MIPS) and estimated (IRS-PUI) pre-explosion fluxes at the position of the SN are summarized in the last row of the table.

[d] Observations at days 1779, 1931 and 2151 were obtained during the *Spitzer* 'warm' mission, where only IRAC 3.6- and 4.5-μm channels were available.

indicated by the downward-pointing arrows. Each waveband demonstrates the decline in brightness from the earliest epochs to around day 800 when the SN has faded or is fading to its faintest levels. At 3.6 and 5.8 μm, the upper limits measured from the difference images indicate that the SN faded to below background levels for ∼200 d. The distinctive rise in brightness after this time (>1000 d) is evident in all wavebands. The latest *Spitzer* data at days 1779, 1931 and 2151 were obtained during the post-cryogenic phase of the mission, where only the shortest wavelength IRAC channels at 3.6 and 4.5 μm were available. They show that sometime between days 1395 and 1779, the mid-IR brightness of the SN at 3.6 and 4.5 μm began to decline again, continuing with a slower decline to day 2151. The 3.6-μm flux at day 2151 is about 9 per cent higher than the pre-explosion level, whilst the 4.5-μm flux at the

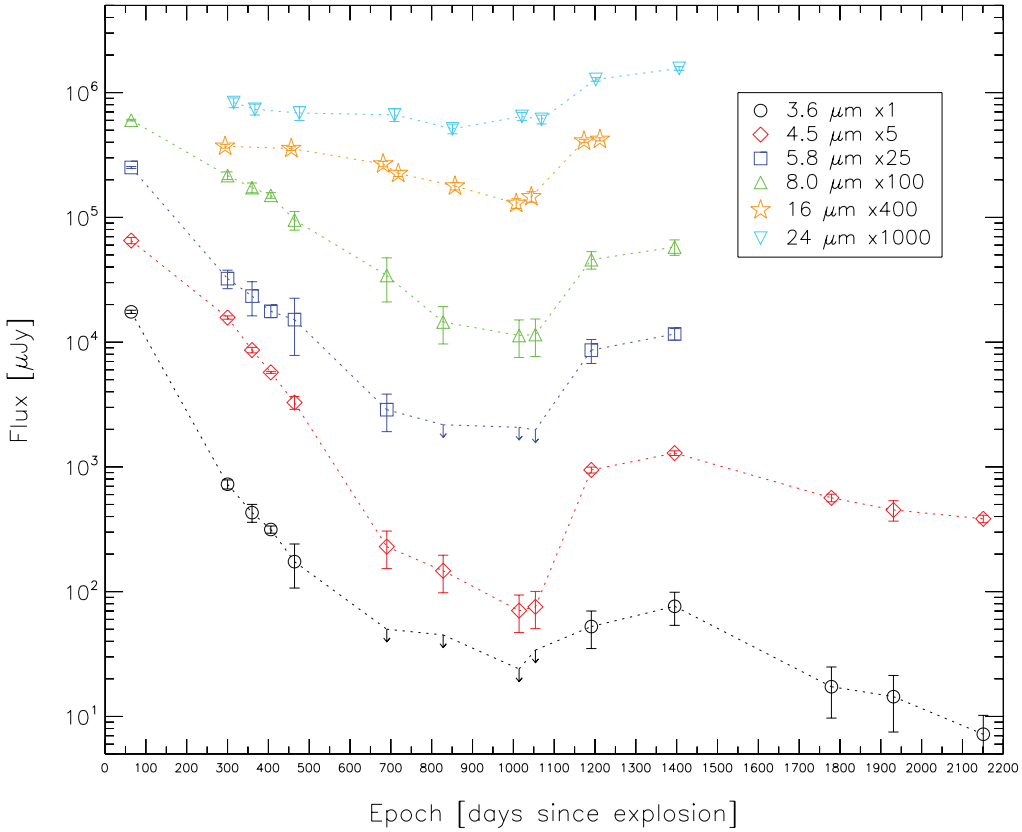

Figure 4. *Spitzer* mid-IR light curves of SN 2004et: 3.6, 4.5, 5.8 and 8.0 μm (IRAC), 16 μm (IRS-PUI) and 24 μm (MIPS). The IRAC and MIPS flux densities are from PSF-fitted photometry carried out on difference images which use the pre-explosion image (day −104 for IRAC and day −75 for MIPS) as the reference image. The 16-μm flux densities are from PSF-fitted photometry of the original images from which an estimated pre-explosion flux was subtracted (see text for details). For non-detections, upper limits to the flux densities are indicated by the downward-pointing arrows. For clarity, the light curves have been shifted vertically by the factors indicated.

latest epoch is a factor of 2.7 brighter than the pre-explosion level. Whilst the 3.6-μm flux densities at days 1779–2151 are lower than the upper limits between days 690 and 1015, the on-source integration times for the later observations were between factors of 3 and 80 longer than those for the earlier observations. The corresponding increase in signal-to-noise ratio for the IRAC 'warm' images, together with difference imaging techniques, allowed the SN to be reliably detected at deeper levels than for previous observations with shorter exposure times when the SN was also faint.

A selection of pre- and post-explosion IRAC images at 4.5, 5.8 and 8.0 μm are shown in Fig. 5, depicting the mid-IR evolution of SN 2004et. The SN position is shown in the pre-explosion SINGS images at day −104, revealing evidence of extended emission in this region. The first mid-IR images of the SN, obtained 64 d after explosion (second row of the figure), showed the SN to be very bright. This was during the photospheric plateau phase which characterizes Type II-P SNe, where hot blackbody emission dominates the optical emission and its Rayleigh–Jeans tail extends into the IR. By day 1015 (third row), it can be seen that the SN has faded to almost pre-explosion levels, but a late rise in brightness is clearly evident by day 1395. Comparable difference images depicting the net mid-IR emission at the SN position for the same epochs are also shown in Fig. 5. The rightmost three boxes in the top row again show the pre-explosion images at day −104, which were used as the reference images for subtraction from the post-explosion images, to yield the difference images shown in the remaining panels. At day 1015 when the SN has faded to its faintest levels, a detection at 4.5 μm can just be discerned. For the same epoch at 5.8 μm, whilst there is positive emission coincident with the position of the SN, this is at a similar level to the average noise levels in the residual background of the difference image and is therefore considered to be a non-detection for which an upper limit to the flux is derived. The SN is much more clearly detected in the 8.0-μm difference image at day 1015, although the irregular residual background, seen as diagonal bands across all of the difference images as this wavelength, creates relatively large uncertainties in the final measured flux.

For the 16-μm *Spitzer*-PUI data, the pre-explosion flux estimated by Kotak et al. (2009) was ∼56 per cent higher than that used here, and so we obtain generally higher post-explosion fluxes than those presented by Kotak et al. (2009). The factor by which our post-explosion fluxes exceed those of Kotak et al. (2009) varies from ∼1.1 to 3.3. The largest differences in the photometry occur for days 1007–1044, when the SN was close to its faintest levels in this waveband. During the final epochs observed (days 1212–1173), when the rebrightening was strongest, the fluxes agree to within 10 per cent.

For the 24-μm *Spitzer*-MIPS data, Kotak et al. (2009) measured the flux in the two SINGS pre-explosion images observed at days −75 and −73, as processed with the standard *Spitzer* pipeline. They found the flux at day −75 to be a factor of almost 1.3 higher than that at day −73. From these, they measured an average pre-explosion flux which is almost 40 per cent lower than the pre-explosion flux measured here. As discussed in Section A1, the pre-explosion MIPS

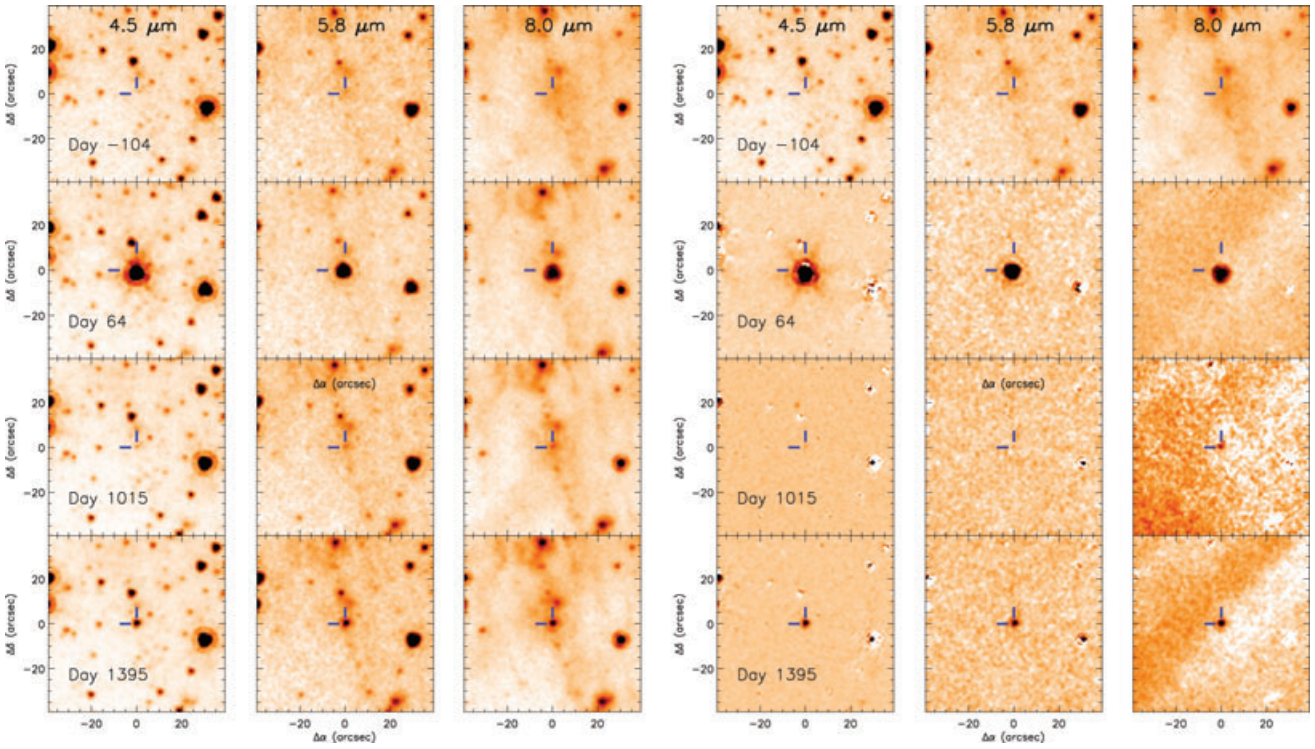

Figure 5. Leftmost three columns: the SN position in *Spitzer* images at selected epochs, showing the mid-IR evolution in IRAC bands 4.5, 5.8 and 8.0 μm. The first row shows the SN field in the pre-explosion SINGS images at day −104. The first mid-IR detections were obtained 64 d after explosion when the SN was still very bright (second row). The third row shows that the SN had faded to almost pre-explosion levels by day 1015, yet by day 1395 the SN has brightened again (fourth row). Rightmost three columns: difference images for the same epochs and wavelengths. The pre-explosion images at day −104 (top row) have been registered to, and subtracted from, the post-explosion images using PSF-matched difference imaging techniques (see Section A1). Note the strong, uneven background residuals at 8.0 μm.

image used here for the analysis of SN 2004et was the SINGS enhanced mosaic from their fifth data delivery, which combined data from both dates. We found a flux consistent with that of Kotak et al. (2009) at day −73, but at day −75 we measured the flux to be about a factor of 1.7 higher. We also measured the fluxes of a number of nearby isolated point sources that were present in both images. No systematic offset was found, with the photometry differing by no more than 1–10 per cent.

Despite measuring a higher pre-explosion flux than Kotak et al. (2009) at 24 μm, we find that photometry from our difference images yielded generally *higher* post-explosion fluxes than theirs. Different techniques/software were used to produce the final difference images, which may have resulted in different background residuals affecting the photometry. In addition, Kotak et al. (2009) used aperture photometry to measure their fluxes, whereas we used PSF-fitting. A comparison between results from aperture photometry and PSF-fitting is presented by Fabbri (2011). In addition, different techniques may have been used to interpolate the 16- and 24-μm data to the IRAC epochs used for the SED analysis.

5 OPTICAL AND NEAR-INFRARED PHOTOMETRY

5.1 The observations

Optical and NIR photometric observations of SN 2004et were obtained as part of the SEEDS programme over the years 2004–09, spanning 79–1803 d after explosion.

The first two epochs of optical photometry were obtained during the plateau phase of the SN at days 79 and 89 with the 32-inch Tenagra II Telescope in Arizona. A further three epochs of optical photometry were obtained during the nebular phase between days 317 and 664 with the GMOS-N in Hawaii. In addition, an archival flux-calibrated Subaru spectrum was used to obtain optical photometry at day 646 by integrating over the *BVRI* filter transmission curves. Two epochs of late-time, high-resolution observations of the SN field were obtained with the *HST* Wide Field Planetary Camera 2 (WFPC2) around 3 years after explosion at days 1054 and 1215. A final epoch of optical photometry, almost 4 years after explosion, was obtained with GMOS-N at day 1412.

The first epoch of NIR photometry was obtained at day 268 with the 2.3-m Bok Telescope, part of the Steward Observatory at Kitt Peak, Arizona. This was followed by three epochs of data from the Near InfraRed Imager (NIRI) on Gemini-North at dates close in time to the optical images taken with GMOS-N during the nebular phase. Late-time, high-resolution data were obtained with the *HST* Near Infrared Camera and Multi-Object Spectrometer 2 (NICMOS2), at epochs corresponding to those of the optical WFPC2 data. A final *H*-band image was taken approximately 5 years (day 1803) after explosion with the WIYN High-resolution InfraRed Camera (WHIRC; Meixner et al. 2010) on the Wisconsin-Indiana Yale NOAO (WIYN) 3.5-m Telescope at Kitt Peak, Arizona.

Table 4 provides a complete log of the optical and NIR photometric observations of SN 2004et taken as part of the SEEDS project. Appendix A2 describes how the optical and NIR data were processed, while Appendix A3 describes our late-time *HST* optical and NIR images which revealed the single point source seen at

Table 4. Log of optical and NIR photometric observations of SN 2004et from the SEEDS collaboration.

Date	Age (d)	Telescope/ instrument	Filters	Exp. time (s)	Programme ID	Principal investigator
2004-12-10	79	Tenagra II 32"	*VRI*	9 × 100	–	D. Welch
2004-12-20	89	Tenagra II 32"	*VRI*	9 × 100	–	D. Welch
2005-06-17	268	Bok 2.3m IR Camera	*JHK*	20 × 30	–	K. Gordon
2005-08-05	317	Gemini GMOS-N	$g'r'i'$	1 × 60	GN-2005B-Q-54	G. Clayton
2005-08-05	317	Gemini NIRI	*JHK*	22 × 30	GN-2005B-Q-54	G. Clayton
2005-10-17	390	Gemini NIRI	*JHK*	10 × 30	GN-2005B-Q-54	G. Clayton
2005-10-31	404	Gemini GMOS-N	$g'r'i'$	1 × 60	GN-2005B-Q-54	G. Clayton
2006-07-06	652	Gemini NIRI	*JHK*	22 × 30	GN-2006A-Q-52	G. Clayton
2006-07-18	664	Gemini GMOS-N	$g'r'i'$	1 × 60	GN-2006A-Q-52	G. Clayton
2007-07-08	1019	*HST* WFPC2	*F606W, F814W*	4 × 400	GO11229	M. Meixner
2007-07-08	1019	*HST* NICMOS2	*F110W, F205W*	5 × 128	GO11229	M. Meixner
2007-07-08	1019	*HST* NICMOS2	*F160W*	4 × 128	GO11229	M. Meixner
2008-01-20	1215	*HST* WFPC2	*F606W, F814W*	4 × 400	GO11229	M. Meixner
2008-01-20	1215	*HST* NICMOS2	*F110W, F205W*	5 × 128	GO11229	M. Meixner
2008-01-20	1215	*HST* NICMOS2	*F160W*	4 × 128	GO11229	M. Meixner
2008-08-04	1412	Gemini GMOS-N	$g'r'i'$	2 × 600	GN-2008B-Q-44	M. Barlow
2009-08-30	1803	WIYN WHIRC	*H*	4 × 180	2009B-0516	M. Otsuka

Table 5. Optical photometry of SN 2004et.

UT date	Age (d)	Magnitudes V	R_c	I_c	Source
2004-12-10	79	13.09 ± 0.04	12.38 ± 0.03	11.93 ± 0.03	Tenagra II
2004-12-20	89	13.21 ± 0.03	12.45 ± 0.03	11.98 ± 0.03	Tenagra II
2005-08-05	317	17.35 ± 0.02	16.52 ± 0.03	15.91 ± 0.04	Gemini GMOS-N
2005-10-31	404	18.28 ± 0.04	17.69 ± 0.03	16.87 ± 0.04	Gemini GMOS-N
2006-06-30	646[a]	21.59 ± 0.55[b]	21.00 ± 0.55[b]	20.63 ± 0.56[b]	Subaru FOCAS
2006-07-18	664	22.13 ± 0.06[b]	21.56 ± 0.09[b]	21.37 ± 0.11[b]	Gemini GMOS-N
2007-07-08	1019	23.20 ± 0.20[c]	–	22.70 ± 0.20[c]	*HST* WFPC2
2008-01-20	1215	23.40 ± 0.30[c]	–	23.00 ± 0.30[c]	*HST* WFPC2
2008-08-04	1412	23.80 ± 0.40[b]	22.87 ± 0.28[b]	22.80 ± 0.70[b]	Gemini GMOS-N
star 2		24.2 ± 0.3	23.5 ± 0.5	22.9 ± 0.4	*HST* WFPC2
Zero-magnitude flux (Jy)		3670.3	2972.3	2402.1	Evans (1993); Glass (1999)
λ_{eff} (μm)		0.55	0.64	0.80	

[a]Optical photometry at day 646 was estimated from an archival Subaru-FOCAS spectrum by integrating over the *BVRI* filter transmission curves. The *B*-band magnitude of SN 2004et at this time was 22.47 ± 0.22, corrected for an estimated *B*-band contribution from star 2 of 25.46 ± 0.50 (see text).
[b]The SN magnitudes at these late epochs have been corrected for contamination by star 2 (whose magnitudes measured from the high-resolution *HST* data are listed in the final table entry).
[c]Since the SN and star 2 were resolved in the day 1019 and day 1215 *HST* images, the magnitudes given for these epochs are for the SN alone.

the SN position in IRAC images to be comprised of at least three sources.

5.2 Photometry and light-curve evolution

The final optical *VRI* magnitudes for SN 2004et are presented in Table 5, including those of neighbouring star 2 discussed previously. The magnitudes for epochs from day 646 onwards have been corrected for the contribution from star 2, but this was not necessary for earlier epochs when the SN brightness dominated. The *B*-band magnitude at day 646, corrected for the contribution from star 2, is detailed in the notes to the table. The NIR *JHK* magnitudes of the SN are given in Table 6, although the magnitudes measured from the NICMOS images at days 1019 and 1215 are *HST* Vegamags (Appendix A2). The optical and NIR light curves are presented in Figs 6 and 7, respectively.

Fig. 6 combines the *BVRI* data of Sahu et al. (2006) with the SEEDS data described above to provide optical light curves (open symbols) from a few days after the explosion to almost 4 years later. The light curves are well sampled until around day 400. Few Type II SNe have been observed beyond ∼500 d. However, SN 1987A, the closest SN to have occurred in the past century, has been well studied for over two decades and provides detailed light curves for comparison. The broad-band *BVRI* light curves of SN 1987A (Hamuy & Suntzeff 1990; Walker & Suntzeff 1991)[2] are plotted as solid curves in Fig. 6, normalized to the data of SN 2004et at around 200 d. The light-curve evolution of both SNe is quite

[2] Hamuy & Suntzeff (1990) data downloaded from the National Optical Astronomy Observatory (NOAO) archive: ftp://ftp.noao.edu/sn1987a/ubvri.txt.

Table 6. NIR photometry of SN 2004et.

UT date	Age (d)	Magnitudes *J*	*H*	*K*	Source
2005-06-17	268	15.14 ± 0.05	15.15 ± 0.03	–[a]	Steward/Bok IR Camera
2005-08-05	317	16.01 ± 0.03	15.84 ± 0.03	15.18 ± 0.04	Gemini NIRI
2005-10-17	390	16.96 ± 0.03	16.62 ± 0.03	16.23 ± 0.04	Gemini NIRI
2006-07-06	652	20.09 ± 0.05	19.52 ± 0.06	19.19 ± 0.07	Gemini NIRI
2007-07-08	1019	22.25 ± 0.13[b]	22.61 ± 0.36[b]	21.91 ± 0.28[b]	*HST* NICMOS
2008-01-20	1215	22.55 ± 0.14[b]	22.69 ± 0.43[b]	21.44 ± 0.18[b]	*HST* NICMOS
2009-08-30	1803	–	≤ 22.6	–	WIYN WHIRC
Zero-magnitude flux (Jy)		1656.3	1070.9	672.8	Glass (1999)
$\lambda_{\rm eff}$ (μm)		1.25	1.65	2.20	

[a]There is no *K*-band magnitude at day 268 as unusual image artefacts compromised the photometry.
[b] *HST* Vegamags in NICMOS2 filters *F110W* ($\simeq J$ band), *F160W* ($\simeq H$ band) and *F205W* ($\simeq K$ band) for days 1019 and 1215. For each filter and epoch, the measured count rate (in units of DN s^{-1}) at the position of the SN was converted to flux by multiplication with the PHOTFNU (Jy s DN^{-1}) conversion factor given in the fits header, where PHOTFNU is the bandpass-averaged flux density for a source that would produce a count rate of 1 DN^{-1}. PHOTFNU $= 1.21 \times 10^{-6}$, 1.50×10^{-6} and 9.69×10^{-7} Jy s DN^{-1} for *F110W*, *F160W* and *F205W*, respectively.

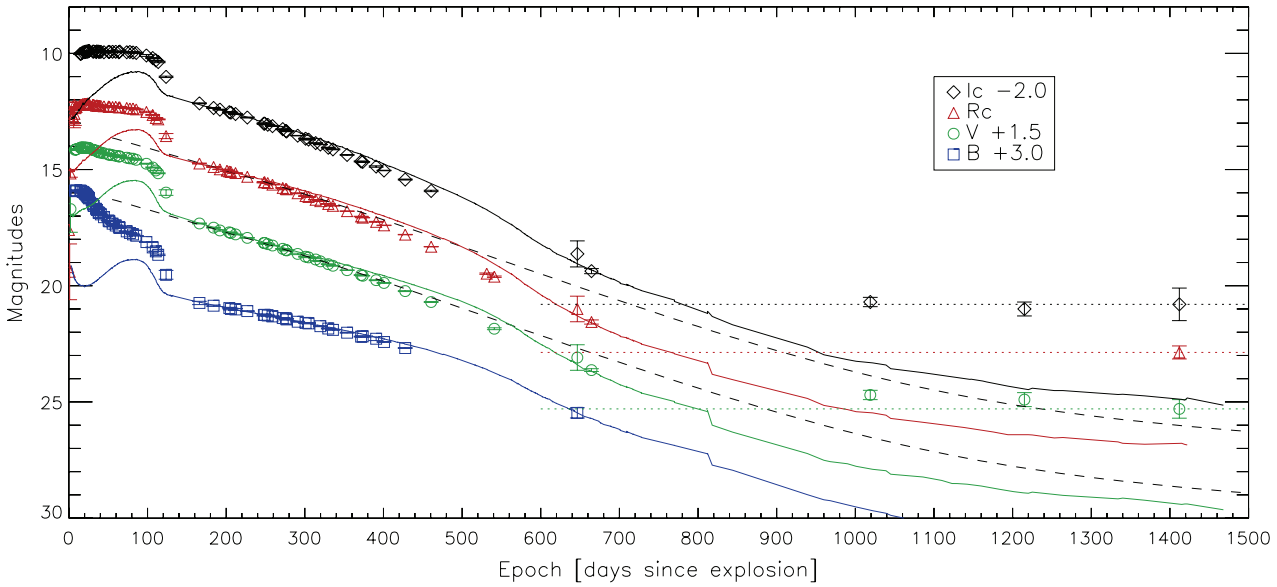

Figure 6. *BVRI* light curves of SN 2004et, based on the data of Sahu et al. (2006) and the SEEDS photometry listed in Table 5. For clarity, the plots have been vertically shifted by the amounts shown in the legend. The black dashed lines are the expected light curves based on the decay of ^{56}Co and other isotopes (Woosley, Hartmann & Pinto 1989) normalized to the *V*- and *R*-band magnitudes of SN 2004et during the early nebular phase (between ∼160 and 260 d). The solid lines are the corresponding light curves of SN 1987A (Hamuy & Suntzeff 1990; Walker & Suntzeff 1991) normalized to those of SN 2004et at ∼200 d. Dotted lines are only to guide the eye along the horizontal or 'flat' parts of the light curve. These curves are typical for every SN that shows a light echo, in that the light curves level off or 'flatten' once the SN flux drops below that of the echo.

similar, from the early nebular phase (∼160 d) to around day 650, although beyond this time their evolution is markedly different. The brightness of SN 2004et clearly levels off from around day 1000 in the *VRI* bands (the last *B*-band measurement was at day 646), while SN 1987A continued to fade. Interestingly, the slope of the radioactive decay curves resemble those of SN 1987A between days ∼720 and 800, around the time when dust production for SN 1987A was assumed to have ended (day 775; Wooden et al. 1993).

For the first few years during the nebular phase, the light curve of Type II SNe is predominantly powered by γ-rays from the radioactive decay of ^{56}Co to ^{56}Fe, at a rate corresponding to the e-folding time of the ^{56}Co decay ($\tau_{56} = 111.3$ d). For example, the *R*-band photometry of the Type II SN 1990E (Benetti et al. 1994) closely follows this evolution through to ∼540 d post-explosion, suggesting that simple ^{56}Co decay provides a good estimate of the unextinguished *R*-band light curve for at least that long. The expected decay rate is γ (mag per 100 d) = 0.98 for complete γ-ray trapping (Patat et al. 1994). For SN 2004et, Sahu et al. (2006) found that the decline of the broad-band *BVRI* magnitudes during the early nebular phase (180–310 d) was linear, with decay rates of $\gamma_B \sim 0.64$, $\gamma_V \sim 1.04$, $\gamma_R \sim 1.01$ and $\gamma_I \sim 1.07$. Maguire et al. (2010) found similar results from their own data (∼136–300 d), with $\gamma_B = 0.64 \pm 0.02$, $\gamma_V = 1.02 \pm 0.01$, $\gamma_R = 0.92 \pm 0.01$ and $\gamma_I = 1.09 \pm 0.01$. With the exception of the *B* band, the decay rates were close to that of ^{56}Co decay, suggesting that γ-ray trapping was efficient during this phase.

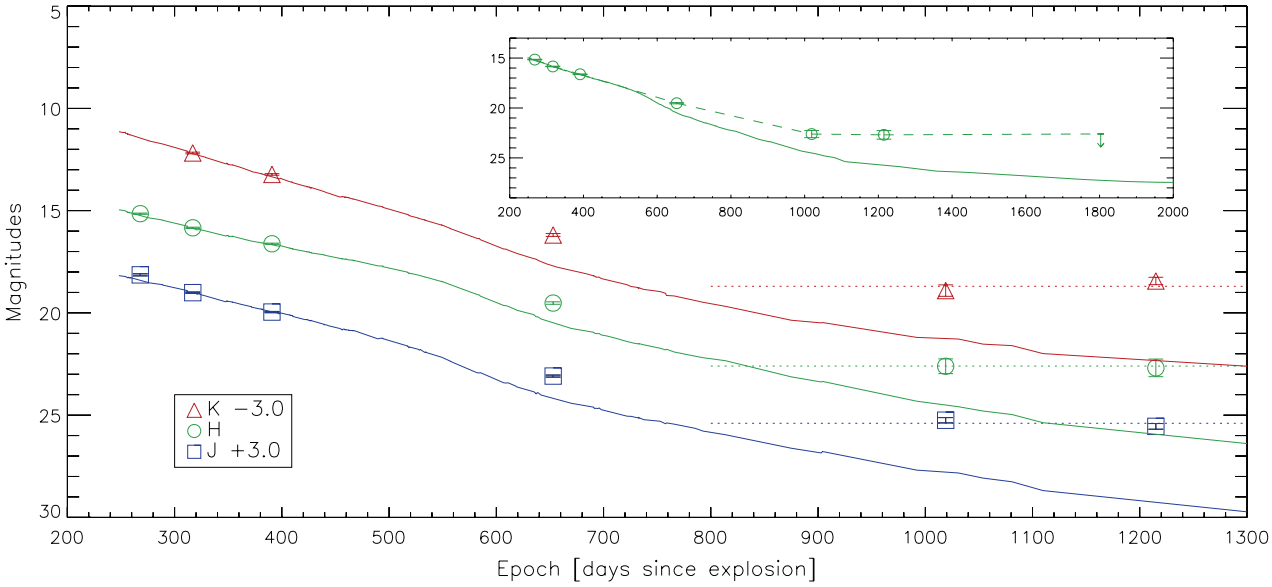

Figure 7. Late-time NIR light curves of SN 2004et, based on the SEEDS photometry listed in Table 6. For clarity, the plots have been vertically shifted by the amounts shown in the legend. The solid lines are the corresponding light curves of SN 1987A (Bouchet & Danziger 1993) normalized to the light curves of SN 2004et at day 317, during the early nebular phase. Dotted lines are only to guide the eye along the horizontal or 'flat' parts of the light curve. The inset shows the *H*-band light curve only for the extended period to day 1803, the final SEEDS NIR observation, taken with the WIYN Telescope in 2009 August. Contamination from neighbouring sources observed in the high-resolution NICMOS images at days 1019 and 1215 resulted in an ambiguous detection of the SN with the WHRIC at day 1803, for which an upper limit (downward-pointing arrow) has been derived.

However, both authors found that the optical decay rates of SN 2004et steepened beyond ∼300 d, suggesting either that the SN had become transparent to γ-rays and hence γ-rays as a source of energy were escaping, or that dust was forming within the ejecta and causing localized optical extinction, or possibly was due to both phenomena.

To investigate this further, we can look again at the radioactive deposition. As the ejecta expand, their opacity to γ-rays is expected to decrease, which results in a modified light curve of the form (Woosley et al. 1989)

$$L^{\gamma}_{56}(t) \propto \mathrm{e}^{-t/\tau_{56}} [1 - \mathrm{e}^{-\kappa_{56}\,\phi_0\,(t_0/t)^2}], \quad (1)$$

where the term in the brackets is the deposition function, i.e. the fraction of γ-rays deposited in the envelope; $\kappa_{56,\gamma} = 0.033\,\mathrm{cm^2\,g^{-1}}$ is the average opacity to ^{56}Co-decay γ-rays, and $\phi_0 = 7 \times 10^4\,\mathrm{g\,cm^{-2}}$ is the column depth at the fiducial time $t_0 = 11.6$ d chosen to match the bolometric light curve of SN 1987A.

After this first source of decay energy has become sufficiently weak, other energy sources which could become important in powering the very late time light curves are γ-rays, positrons and electrons from the radioactive decay of ^{57}Co, ^{44}Ti and ^{22}Na. The equations that describe the energies from all these isotopes, including ^{56}Co, were summarized by Li, McCray & Sunyaev (1993), following the work of Woosley et al. (1989), to describe the deposition behaviour of SN 1987A. Adopting the same deposition behaviour for SN 2004et, the radioactive decay curve attributable to the energy sources from these isotopes, including a term to account for the decrease in opacity to γ-rays as the ejecta expands, has been plotted in Fig. 6 (dashed line) over both the *V*- and *R*-band magnitudes of SN 2004et, normalizing to the early nebular phase data (∼160–260 d). As expected, with the exception of the *B* band, the decay rates during the early nebular phase closely follow those of the radioactive decay deposition. However, from about 400 d the *R*-band light curve has clearly begun to decline more rapidly than the expected light curve from radioactive decay deposition. The *I* band follows a similar trend, whereas the steepening of the decline rate appears to occur slightly later in the *V* band, having clearly begun sometime between 460 and 540 d. In comparison with the expected radioactive decay deposition behaviour of SN 1987A, as modelled by Li et al. (1993), there is evidence for a steepening decline of the light curves, indicative of dust formation in the ejecta of SN 2004et from around 400 d, and possibly earlier (Sahu et al. 2006; Maguire et al. 2010). From the *V*-band light curve (Fig. 6), we estimate that the difference between the observed and predicted light curves was 0.8 mag by day 690, if allowance is made for the effective opacity term for ^{56}Co γ-rays, or 1.5 mag if this term is neglected.

It is clear that the elevated brightness of SN 2004et after 1000 d cannot be explained by the inclusion of isotope decays, such as ^{57}Co and ^{44}Ti, which could be important at these late times. The plateauing of the optical light curves above the expected radioactive decay suggests an additional energy source has come into play by at least day 1000 and is consistent with the late rise observed in the mid-IR observations after this time. Similar phenomena observed for other SNe have been attributed to light echoes (e.g. SN 2007od; Andrews et al. 2010).

Fig. 7 presents the late-time NIR light curves (open symbols) of SN 2004et based on the SEEDS data described previously. The *JHK* light curves of SN 1987A (solid lines; Bouchet & Danziger 1993) have been arbitrarily scaled to the early nebular phase data of SN 2004et for comparison. The NIR light curves of SN 2004et are not well sampled but clearly deviate from those of SN 1987A by day 646, after which time SN 2004et is systematically brighter. The NIR light curve evolution reflects that of the optical, with a relative plateau in brightness occurring from around 1000 d, consistent with a light echo hypothesis.

However, by day 1803 (see inset in Fig. 7), the *H*-band brightness has faded to beyond a clear detection with the WHRIC detector on the 3.5-m WIYN Telescope. The derived upper limit of 22.6 mag

accounts for contamination by neighbouring stars (as described in Section A2) and suggests the SN faded sometime after day 1215.

6 SPECTRAL ENERGY DISTRIBUTION ANALYSIS BASED ON OPTICAL, NIR AND MID-IR PHOTOMETRY

The mid-IR photometry listed in Table 3, along with the optical and IR photometry in Tables 5 and 6 and the optical photometry of Sahu et al. (2006), has been used to investigate the SED of SN 2004et at each of the IRAC observation epochs from days 64 to 1395.

6.1 Blackbody fitting

To investigate the physical processes that determine the observed optical and IR continuum emission and their evolution, blackbodies were matched to the SEDs at each of the IRAC epochs from day 64 to 1395. Where necessary, the light curves for the optical, NIR, PUI 16-μm and MIPS 24-μm data were used to interpolate their measured flux densities to the epochs of the IRAC data. It should be noted that to extrapolate the last *B* magnitude, obtained on day 646 to the closest IRAC epoch at day 690, the better sampled *V*-band decline rate during this period was adopted in order to account for the gradual flattening of the light curve. Similarly, the *JHK* magnitudes from day 652 were extrapolated to the closest IRAC epoch of day 690 assuming the decline rate observed in the I_c band during this period. Gemini-Michelle flux densities at 11.2 μm were not interpolated due to insufficient data, but, where available, they are compared with the closest IRAC epoch.

The interpolated optical data were converted from the standard Johnson–Cousins BVR_cI_c magnitudes to flux densities using the zero-magnitude flux densities of Evans (1993) and Glass (1999). The interpolated Steward and Gemini NIR data were converted from standard *JHK* magnitudes to flux densities using the zero-magnitude flux densities of Glass (1999). The late-time *HST*-NICMOS flux densities were obtained by multiplying the count rate measured for the SN by the PHOTFLAM (erg cm^{-2} Å^{-1} DN^{-1}) conversion factor from the fits image headers, where PHOTFLAM is the bandpass-averaged flux density in F_λ for a source that would produce a count rate of 1 DN s^{-1}. All flux densities were dereddened using $E(B-V) = 0.41$ mag (Zwitter et al. 2004) and assuming the extinction law of Cardelli, Clayton & Mathis (1989) with $R_V = 3.1$, corresponding to $A_V = 1.27 \pm 0.22$ mag.

6.1.1 Day 64

Panel (a) of Fig. 8 shows a fit to the SED at day 64, during the photospheric plateau phase of SN 2004et. The fit, which uses a 5400-K blackbody normalized to the IRAC 5.8-μm flux density, underestimates the *V*- and *R*-band flux densities, which we attribute to the presence of strong emission lines such as Hα in the 5400–7000 Å wavelength region (Sahu et al. 2006; Kotak et al. 2009), while it significantly overestimates the *U*-band flux density. A spline curve fitted to the *UB* photometry was therefore used to estimate the total flux shortwards of *B*. This spline curve was combined with the 5400-K blackbody, truncated at wavelengths $\leq B$ (4400 Å), to yield a total integrated flux of 4.5×10^{-13} W m^{-2} (with a corresponding luminosity of 4.9×10^8 L$_\odot$), about 93 per cent of the total integrated flux/luminosity from the hot blackbody alone. At wavelengths $\leq B$, the total flux corresponding to the spline fit constituted about 49 per cent of that from the 5400-K blackbody fit. In panel (a) of Fig. 8 the solid line represents the combined spline and truncated blackbody fit, whilst Table 7 lists the parameters for the blackbody fits.

It is well known that all Type I SNe show a pronounced early-time deficit at ultraviolet (UV) wavelengths relative to a blackbody fitted at longer wavelengths (e.g. Panagia 2003). This has been interpreted as due to strong line blanketing by many low-excitation lines of Fe II and other lines shortwards of ∼4000 Å (e.g. Branch & Venkatakrishna 1986). The situation for Type II SNe seems to be less clear. In his review of optical spectra of SNe, Filippenko (1997) noted that most Type II SNe do not show this feature, with the early-time spectra approximating a single-temperature Planck function from UV through to IR wavelengths, and occasionally even showing a slight UV excess. However, Fransson et al. (1987), from their studies of the peculiar Type II SN 1987A, concluded that SN atmospheres with a normal (solar) chemical composition can give rise to line blanketing effects, such as those seen in the UV spectra of SN 1987A. They proposed that the differences in UV spectra of SNe may instead be due to differences in the density of the CSM. The earliest *International Ultraviolet Explorer* (1150–3200 Å) spectra of SN 1987A (∼6 d after explosion) showed a strong UV deficit in the wavelength range ∼1250–3200 Å, relative to the 6000-K blackbody curve defined at optical and IR wavelengths (Danziger et al. 1987). This was still present at day 60, and possibly as late as day 260, as shown by the best-fitting SEDs of Wooden et al. (1993). The apparent UV drop-off relative to the blackbody fit to the photometric SED of SN 2004et at day 64 suggests that a similar effect is present in this Type II-P SN. Li et al. (2005) noted from a spectrum of SN 2004et at day 9 that 'there is a peculiar decline bluewards of 4000 Å not commonly observed in the spectra of normal SNe II-P'.

6.1.2 Days 300–828

The blackbody fits to the SEDs at days 300–828 are shown in Fig. 8. The corresponding blackbody parameters are listed in Table 7. For each epoch, more than one component was required to obtain a reasonable fit to the optical, NIR and mid-IR photometry. These were comprised of (i) a hot blackbody, with temperatures during the period 300–828 d ranging from 7100 to 10 000 K, representing the optical and NIR continuum emission from the optically thick hot gas of the ejecta, (ii) a warm blackbody (420–650 K) representing the emission at mid-IR wavelengths and (iii) from day 464 onwards, a cooler (200–250 K) blackbody to account for the observed emission at the two longest mid-IR wavelengths (16 and 24 μm). Excess emission is also present at 24 μm on days 300–406, but at a relatively constant level (see Fig. 8).

From days 300 to 464, the mid-IR emission demonstrated a clear excess at 4.5 μm, as noted by Kotak et al. (2009). A similar feature has been seen in mid-IR photometry of other Type II SNe, such as the Type II-P SN 2003gd at day 499 (Sugerman et al. 2006) and SN 2007it at day 340 (Andrews et al. 2010). This can be attributed to emission from the carbon monoxide (CO) fundamental band at 4.65 μm, which was directly observed in the IR spectra of the Type IIpec SN 1987A from as early as 100 d after explosion (Suntzeff & Bouchet 1990) and stayed visible until at least day 615 (Wooden et al. 1993). The red wing of the same emission line was detected in the *Spitzer* IRS spectra of the Type II-P SN 2004dj at days 109 and 129 (Kotak et al. 2005). Together with the detection of the first overtone of CO at ∼2.3 μm in the NIR spectrum of SN 2004et (Maguire et al. 2010), as well as in the spectra of several other

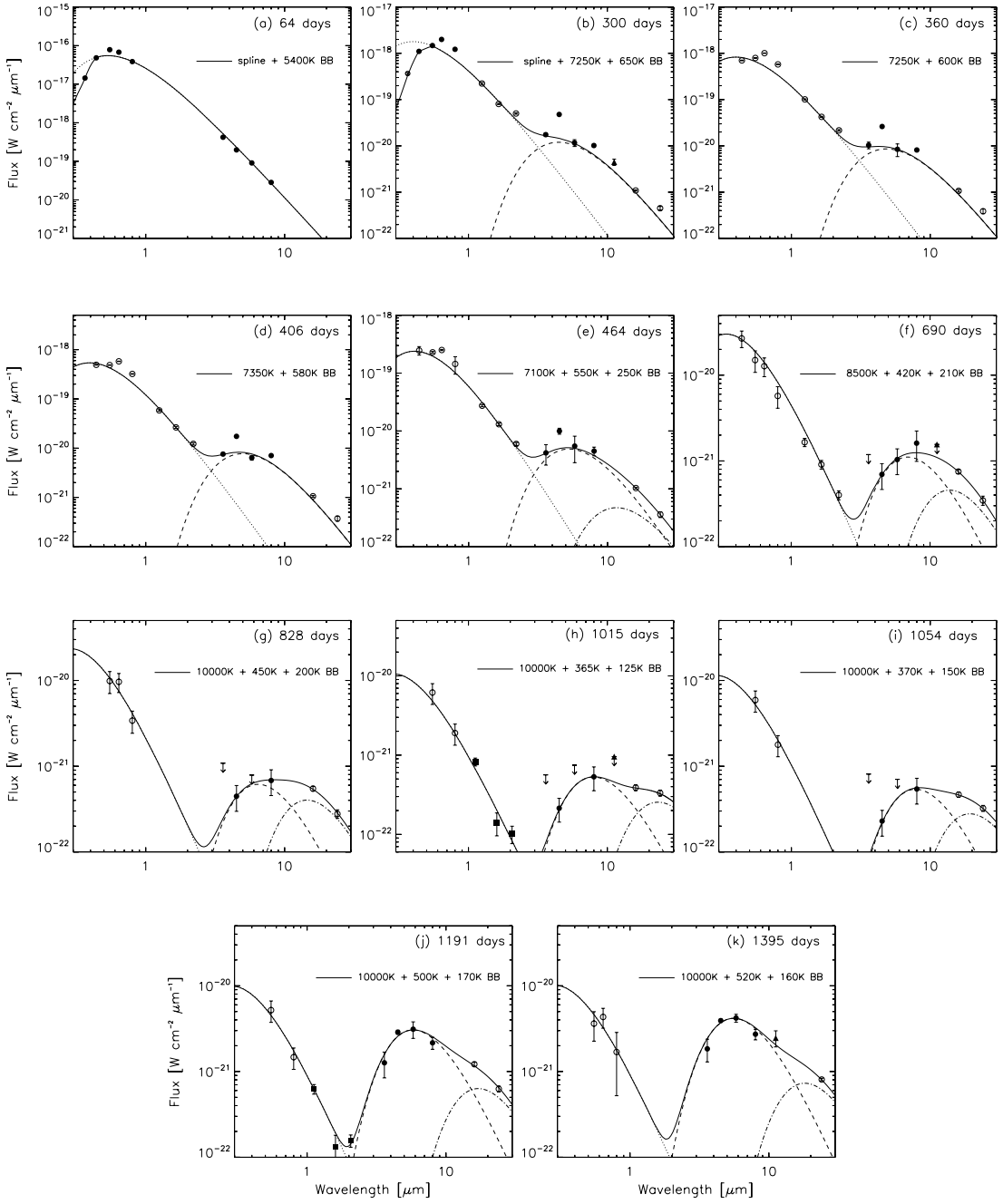

Figure 8. Blackbody fits to the day 64–1395 SEDs of SN 2004et as defined by the optical–IR observations (wavelength range plotted: 0.3–30 μm). Filled circles indicate fluxes observed at the epoch of the IRAC observations. Open circles indicate optical, NIR and mid-IR photometry which has been interpolated or extrapolated to the epochs of the IRAC observations. Filled squares indicate the closest epoch (i.e. not interpolated) *HST*-NICMOS photometry and filled triangles indicate the closest epoch Gemini-Michelle N′-band photometry (see Table 2 for epochs of the Michelle and NICMOS observations). Upper flux limits for non-detections are indicated by the downward-pointing arrows. Where error bars are not shown, uncertainties are smaller than the symbol size. All flux densities were dereddened using $E(B-V) = 0.41$ mag (Zwitter et al. 2004) and the extinction law of Cardelli et al. (1989) with $R_V = 3.1$.

Type II SNe (Gerardy et al. 2002, and references therein), these observations indicate that strong CO emission is common in Type II SNe.

Kotak et al. (2009) also noted an excess at 8.0 μm compared to blackbodies matched to the mid-IR continuum emission from days 300 to 690. They found this to be consistent with a broad emission feature between 8 and 14 μm seen clearly in *Spitzer* IRS spectra until at least days 450–481 and attributed this to silicate emission, with a contribution from the silicon oxide (SiO) fundamental band in the 7.7–9.5 μm region. Accordingly, our warm blackbody component was normalized to the 3.6- or 5.8-μm fluxes as best representing the continuum emission during these times. For the best-fitting SED at day 300 [panel (b) in Fig. 8], the Gemini 11.2-μm flux from day 311 is also underestimated by the warm blackbody component. This excess is attributed to the broad silicate emission feature seen at its strongest in the IRS spectra at days 294 and 349 presented by Kotak et al. (2009). The 8.0-μm excess is no longer evident after day 690, consistent with the IRS spectrum at day 823 presented by

Table 7. Blackbody-fitted parameters to the SEDs of SN 2004et.[a]

Epoch (d)	T_{hot} (K)	F_{hot} (10^{-15} W m^{-2})	R_{hot} (10^{15} cm)	v_{hot} (km s^{-1})	L_{hot} (10^6 L$_\odot$)	T_{warm} (K)	F_{warm} (10^{-15} W m^{-2})	R_{warm} (10^{15} cm)	v_{warm} (km s^{-1})	L_{warm} (10^6 L$_\odot$)	T_{cool} (K)	F_{cool} (10^{-15} W m^{-2})	R_{cool} (10^{15} cm)	v_{cool} (km s^{-1})	L_{cool} (10^6 L$_\odot$)	F_{tot} (10^{-15} W m^{-2})	L_{tot} (10^6 L$_\odot$)
64[b]	5400	446	1.75	3167	485	–	–	–	–	–	–	–	–	–	–	446	487[b]
300[c]	7250	10.9	0.15	59	11.9	650	0.81	5.16	1989	0.89	–	–	–	–	–	11.7	12.8[c]
360	7250	5.04	0.10	33	5.50	600	0.63	5.34	1718	0.69	–	–	–	–	–	5.67	6.19
406	7350	3.24	0.081	23	3.54	580	0.59	5.51	1570	0.68	–	–	–	–	–	3.83	4.18
464	7100	1.48	0.058	15	1.62	550	0.39	4.99	1246	0.42	250	0.083	11.15	2782	0.091	1.96	2.13
690	8500	0.16	0.013	2.2	0.17	420	0.12	4.67	784	0.13	210	0.096	16.96	2845	0.10	0.37	0.40
828	10000	0.10	0.0078	1.1	0.11	450	0.060	2.93	409	0.065	200	0.089	17.99	2515	0.096	0.25	0.27
1015	10000	0.047	0.0052	0.60	0.051	365	0.064	4.59	523	0.069	125	0.090	46.36	5286	0.098	0.20	0.22
1054	10000	0.050	0.0054	0.60	0.055	370	0.064	4.47	491	0.070	150	0.082	30.72	3374	0.089	0.20	0.21
1191	10000	0.044	0.0050	0.49	0.047	500	0.27	5.02	487	0.29	170	0.16	33.87	3291	0.18	0.48	0.52
1395	10000	0.045	0.051	0.42	0.049	520	0.35	5.32	441	0.39	160	0.20	42.33	3512	0.22	0.60	0.65

[a]Up to three components – hot, warm and cool – were used to fit the continuum emission of the SEDs (see text). For each component, R is the blackbody radius corresponding to the best-fitting temperature, T, v is the expansion velocity corresponding to the radius R and L is the luminosity for an adopted distance to the SN of 5.9 Mpc.

[b]The day 64 5400-K blackbody fit overestimated the U-band flux. A spline curve fit to the UB fluxes and extrapolated to shorter wavelengths was combined with the 5400-K blackbody fit to the longer wavelength data, where the blackbody was truncated at wavelengths shorter than the B band – see panel (a) of Fig. 8. The total integrated flux and corresponding luminosity of this 'spline + 5400 K blackbody' fit are about 93 per cent of those values for the pure 5400-K blackbody fit shown in this table.

[c]At day 300, it was found that the hot component blackbody still overestimated the fluxes at the shortest wavelengths. A spline curve fit to the UBV fluxes and extrapolated to shorter wavelengths was combined with the two-component blackbody fit to the longer wavelength data, as shown in panel (b) of Fig. 8, where the 7250-K blackbody component was truncated at wavelengths shorter than the V band. The total integrated flux and corresponding luminosity of this 'spline + 7250 K + 650 K blackbody' fit are about 73 per cent of those values for the combined 7250 K + 650 K blackbody fit shown in this table.

Kotak et al. (2009). Panel (g) of Fig. 8 shows that by day 828, the observed 8.0-μm flux is well matched by the blackbody fits.

6.1.3 *Days 1015–1395*

Best fits to the SEDs at epochs of days 1015, 1054, 1191 and 1395 are also shown in Fig. 8, and the corresponding blackbody parameters are listed in Table 7. Hot (10 000 K), warm (350–520 K) and cool (120–170 K) blackbody components were matched to the optical, NIR and mid-IR photometry. For days 1015 and 1191, the adopted NIR fluxes were those measured in the *F110W*, *F160W* and *F205W* NICMOS2 filters at the reasonably contemporary epochs of days 1019 and 1215.

6.2 Discussion of results from blackbody fitting

The complete set of parameters from the blackbody fits to the photometry from days 64 to 1395 are listed in Table 7. The temperature evolution of the best-fitting multicomponent blackbodies is shown in Fig. 9.

The left-hand panel of Fig. 10 shows the evolution of the luminosities of each of the blackbody components, and their sum, compared with the theoretical luminosity due to the radioactive deposition of ^{56}Co, ^{57}Co, and other isotopes, adopting the deposition behaviour of SN 1987A as modelled by Li et al. (1993) and Woosley et al. (1989). The radioactive decay deposition curve for SN 1987A was scaled by a factor of 0.69 to normalize it to the total luminosity of SN 2004et between days 300 and 464. It should be noted that the blackbody fits to the photometry mainly trace the continuum emission of the SN (known optical and mid-IR emission-line features were deliberately not matched by the blackbodies as discussed in the previous sections). As a consequence, the luminosities listed in Table 7 slightly underestimate the total luminosities.

Figure 9. The temperature evolution of the blackbody components that were fitted to the SED of SN 2004et at different epochs. Hot component temperatures ranged from 5400 to 10 000 K, warm component temperatures ranged from 370 to 650 K and cool component temperatures ranged from 125 to 250 K (see Table 7).

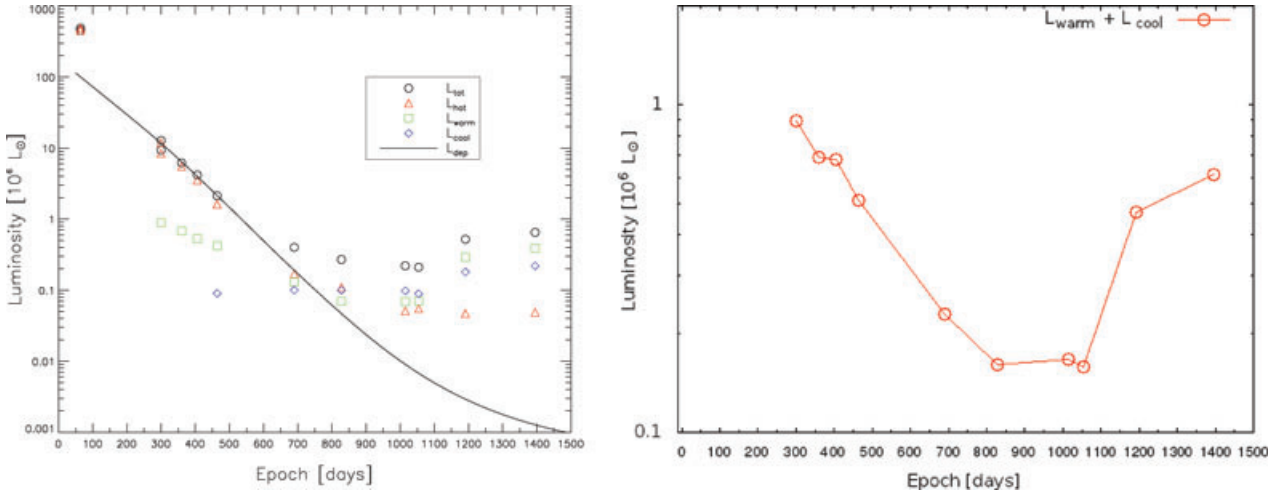

Figure 10. The luminosity evolution of SN 2004et, from multicomponent blackbody fits to the SED at each epoch (see Table 7). The temperature evolution of the individual components is shown in Fig. 9. Left: the luminosity evolution of the individual components (hot, warm and cool) is shown at each epoch, together with that of the corresponding total luminosity. The solid curve shows the predicted luminosity due to radioactive deposition, as scaled from the models of Li et al. (1993; see text for details). Right: the sum at each epoch of the luminosities of the two components, warm and cool, attributed to dust emission, showing a steady decline up to day 828, followed by a subsequent rise.

6.2.1 Evolution of the hot component

The day 64 photometry can be fitted by a 5400-K blackbody, consistent with an origin from the optically thick emission of the ejecta photosphere, with the Rayleigh–Jeans tail of the corresponding blackbody extending into the IR. As the ejected envelope adiabatically expands and cools, the hydrogen ionized by the initial SN shock approaches the temperature for recombination (∼5000 K) and a recombination wave recedes through the envelope. The recombination front defines the photosphere and as such the temperature of the photosphere is characterized by the recombination temperature of hydrogen. Wooden et al. (1993) found that a hot component of 5000–5500 K was a good match to the SED of SN 1987A from days 60 to 777, which they found to be in agreement with observations of other Type II SNe by Kirshner et al. (1973). With a similar temperature, the 5400-K blackbody fit shown in panel (a) of Fig. 8 is representative of the photospheric continuum emission at this time. The ejecta velocity of 3167 km s^{-1} implied by the emitting radius of the 5400-K blackbody is in reasonable agreement with the velocity of ∼3500 km s^{-1} found by Sahu et al. (2006) for SN 2004et in the plateau phase, estimated from the minimum of weak, unblended absorption lines of Fe II at 4924, 5018 and 5169 Å. Kotak et al. (2009) obtained a reasonable fit to the day 64 SED of SN 2004et with a single 5300-K blackbody, concluding there was little sign of thermal emission from dust.

As expected, the corresponding luminosity at day 64 exceeds that from radioactive decay deposition, which only begins to dominate the light curve during the nebular phase (from ∼130 d; Maguire et al. 2010), following the sharp decline from the plateau at ∼110 d (Sahu et al. 2006). For the 5400-K blackbody fit, the day 64 luminosity exceeds that from radioactive deposition by a factor of 4.9, or by a factor of 4.5 if considering the spline plus truncated blackbody fit which is a better match to the *U*-band data. This compares to the factor of 3.8 found by Kotak et al. (2009).

By day 300, the estimated temperature of the hot blackbody component had increased to 7250 K and then remained relatively constant (±∼150 K) until day 464 (Fig. 9), whilst its luminosity faded quite rapidly (by a factor of ∼7) during this time (Fig. 10). Note that at day 300, the blackbody fit significantly overestimates the fluxes at the shortest wavelengths in the *U* and *B* bands, as also seen at day 64 (see previous discussion). By day 690, the temperature had increased again to 8500 K and to 10 000 K by day 828, whilst the luminosity continued to decrease (by a factor of ∼15). For epochs beyond 1000 d, the temperature of the hot component appears to remain constant.

6.2.2 Evolution of the warm and cool dust components

The warm dust component cooled monotonically from 650 to 420 K between days 300 and 690 (Fig. 9). This is consistent with the fading of SN 2004et observed in the mid-IR during this time. The sum of the luminosities of the hot and warm components is less than or comparable to the predicted radioactive deposition up to day 690. On day 828, however, the sum of the hot and warm component luminosities was a factor of 1.7 higher than the predicted radioactive deposition luminosity.

The presence of a mid-IR excess from day 300, demonstrated by the requirement of a warm component to match the SEDs from this time, and the evolution of this warm component from 300 to 690 d are consistent with emission from dust freshly synthesized in the SN ejecta, in agreement with the results of Kotak et al. (2009) from their interpretation of similar data.

The approximately constant luminosity of the warm component between days 828 and 1054 corresponded to the lowest level reached, since at day 1191 the warm component luminosity had increased by a factor of 4.3. From day 1015, the warm component luminosity clearly exceeds that of the radioactive deposition (by a factor of ∼8) and at day 1191 by a factor of over 100.

The cool dust component, required to fit the mid-IR fluxes longwards of 16 μm from day 464 onwards, showed a monotonic decline in temperature from 250 K at day 464 to ∼120 K at day 1015, but then increased slightly and remained around 160 K between days 1054 and 1395. Its luminosity stayed roughly constant from days 464 to 1054, but had increased by a factor of ∼2 by days 1191–1395. The velocities implied by the minimum emitting radii of these cooler blackbodies ranged from ∼2500 to 6000 km s^{-1}.

Table 8. Input parameters for R^{-2} density distribution dust models.

	Diffuse source							Smooth		Clumpy	
Epoch (d)	R_{in} (10^{15} cm)	R_{out}/R_{in}	L (10^6 $L_\odot$)	T (K)	AC:sil (per cent)	a_{min}–a_{max} (μm)	$n(a)\propto a^{-p}$ p=	$\tau_{0.55}$	M_d (10^{-5} $M_\odot$)	$\tau_{0.55}$	M_d (10^{-5} $M_\odot$)
300	7.0	4.0	12.8	8000	20:80	0.1–1.0	3.5	0.11	3.8	0.07	7.6
360	6.0	4.5	6.19	7000	20:80	0.1–1.0	3.5	0.20	5.6	0.12	10.0
406	7.0	4.0	4.18	8000	20:80	0.1–1.0	3.5	0.18	6.5	0.24	22.4
464	8.0	4.0	2.13	8000	20:80	0.1–1.0	3.5	0.38	11.1	0.39	50.0
690	6.0	3.5	0.40	8000	20:80	0.1–1.0	3.5	1.30	43.9	1.31	150

Kotak et al. (2009), on the other hand, found that the temperature of their cool component remained approximately constant, at 120 ± 10 K for all epochs from day 300–1395, with minimum blackbody radii corresponding to velocities as large as 12 000 km s^{-1}, so they ruled out ejecta-condensed dust as a source of the cool dust emission. The differences between our results for the cool component and those of Kotak et al. (2009) are most likely due to the differences in the photometry at the longest wavelengths, 16 and 24 μm, as discussed in Section 4.2. Our 16- and 24-μm fluxes required generally higher temperature blackbodies to fit them than did those of Kotak et al. (2009). Since our luminosities for the cool component are generally consistent with those of Kotak et al. (2009), the higher blackbody temperatures that we obtain resulted in lower minimum radii and therefore lower minimum outflow velocities.

The right-hand panel of Fig. 10 shows the evolution of the sum of the luminosities of the two dust components (warm plus cool). It shows a steady decline until day 828, a period of constant luminosity until day 1054 and a steep rise thereafter. The evolution beyond day 828 implies the presence of an additional energy source. Kotak et al. (2009) found similar results and interpreted the late rise in the mid-IR flux as due to ejecta–CSM interaction and the subsequent formation of a cool dense shell of dust behind the reverse shock of the SN. An alternative explanation in terms of a light echo from pre-existing extended CSM dust will be presented by Sugerman et al. (in preparation).

7 RADIATIVE TRANSFER MODELLING: DAYS 300–690

In agreement with previous investigators (Sahu et al. 2006; Kotak et al. 2009), the development of a red–blue asymmetry in optical emission-line profiles, the evidence from optical light curves for additional extinction by dust in the ejecta and the development of a mid-IR excess attributable to dust emission all support the inference that dust formed within the ejecta of SN 2004et from about 300 d after explosion. As discussed above, by day 828 the total luminosity exceeded the estimated radioactive deposition luminosity by a factor of 4 (Fig. 10), indicating that an additional component dominated by that date. Consequently, epochs later than day 690, when the thermal IR emission can no longer be solely attributed to internally heated newly formed dust in the ejecta, will not be modelled here – Sugerman et al. (in preparation) will present a circumstellar light echo model for these later epochs.

To investigate the time evolution of dust formation in the ejecta of SN 2004et and to estimate the mass of dust present, a number of dust shell models were built to match the observed SEDs at the epochs between days 300 and 690 (Table 8). The models were calculated using the 3D Monte Carlo RT code MOCASSIN (Ercolano et al. 2003; Ercolano, Barlow & Storey 2005) which accounts for the primary and secondary components of the radiation field in a fully self-consistent manner through absorption, re-emission and scattering of photons. The photon paths are followed from a specified source through a given composition, grain-size distribution, density and geometry of dust. The particular choices of these parameters are either constrained a priori or are varied until the model emission and extinction match the observations.

Table 9. The contribution from line emission to the *VRI* bands.

Epoch (d)	V (per cent)	R (per cent)	I (per cent)
336	21	75	68
417	20	58	60
454	26	58	57
649	26	60	27

For the day 300–690 models, we assumed that the observed IR emission originated from dust formed in the SN ejecta. Heating is due to γ-rays from the decay of ^{56}Co, which are reprocessed to optical and UV wavelengths through interaction with the gas. We assume that this leads to a local radiation field whose strength is proportional to the local ejecta density. Based on these assumptions, and following the previous modelling of SN 2003gd by Sugerman et al. (2006) and of SN 1987A by Ercolano et al. (2007), the RT models were constructed such that the dust and source luminosity were mixed within a spherical expanding shell of inner radius R_{in} and outer radius $R_{out} = YR_{in}$. For the dust density distribution, we considered two cases: (i) a smooth distribution following an r^{-2} density profile (smooth model) and (ii) a clumpy model where dense clumps exist in a less dense interclump medium (ICM), where the ICM follows a smooth r^{-2} density distribution, with the local heating source located only in the ICM. For each case, we compared the observed SEDs with those reproduced by the models to determine which gave the best fit to the observations.

Before running the models, we estimated the contribution from line emission to the *VRI* bands. We used day 417 and 454 optical spectra downloaded from SUSPECT plus day 336 TNG and day 646 Subaru spectra, along with the Subaru/FOCAS *VRI*-band filter transmission curves[3] because these have similar band centres and widths to the standard Johnson filters. The percentage line contributions in each band are listed in Table 9. When evaluating the fitting accuracy of the SED modelling, we excluded the *R* and *I* bands on days 300, 360, 406 and 464 because both bands were dominated by line emission at those epochs. We also omitted the IRAC 4.5-μm

[3] See http://www.naoj.org/Observing/Instruments/FOCAS/camera/filters.html.

data points from the fitting, due to the potentially very large CO line emission contributions in that band (Kotak et al. 2009). Although our modelling took into account potential emission from the broad silicate 10-μm band, the SiO fundamental vibrational band can also contribute to the IRAC 8-μm band – from *Spitzer* IRS spectra its contribution was deduced by Kotak et al. (2009) to be significant on days 300–464.

7.1 Smooth dust distribution models

Both amorphous carbon (AC) and silicate dust grains were considered. Optical constants were taken from Zubko et al. (1996) for amorphous carbon (their ACH2) and from Draine & Lee (1984) for the silicates. To investigate the dust composition, models were run with amorphous carbon:silicate mixtures of $(100 - x)$:x per cent, for $x = 0, 20, 40, 60, 80, 100$. It was found that the case of 20 per cent amorphous carbon and 80 per cent silicate (by mass) best matched the observed SEDs at all epochs, and this composition was adopted for all subsequent models.

A standard MRN $a^{-3.5}$ distribution (Mathis, Rumpl & Nordsieck 1977) with $a_{\rm min} = 0.005$ μm and $a_{\rm max} = 0.25$ μm could not reproduce the steepness of the observed SED in the *JHK* bands before day 690, nor the 16- and 24-μm flux densities. An improved fit was found using an MRN distribution with $a_{\rm min} = 0.1$ μm and $a_{\rm max} = 1.0$ μm, and this was subsequently adopted for all epochs.

The density distribution in SN ejecta can range from approximately flat to very steep in the layers that had formed the photosphere of the progenitor. Here, we adopt an r^{-2} law. We found that distributions steeper than r^{-3} led to too much emission in the 1.6–3.6 μm spectral region at the earlier epochs, as a result of the high densities and high heating rates at the inner edge of the ejecta. As a first guess, we adopted initial values for $R_{\rm in}$ from our blackbody fitting, and then varied them to match the observations. We calculated models with shell size scaling parameters $Y = R_{\rm out}/R_{\rm in} = 3.0, 3.2, 3.5, 4.0, 4.5$. The adopted heating luminosities were the total luminosities measured from the blackbody fitting at each epoch, as listed in the final column of Table 7. Table 8 lists the parameters of the best-fitting models for each epoch, including derived dust masses, $M_{\rm d}$, and visual optical depths $\tau_{0.55}$. The variation in derived dust masses when parameters such as $R_{\rm in}$, Y, L and T are varied from their best-fitting value allows us to estimate that the uncertainty in the derived dust mass is ≤50 per cent. Fig. 11 plots the emergent SEDs (red solid lines) and the observations, where the plotted flux densities have been corrected for foreground extinction.

The observed SEDs were best fitted using diffuse field radiation temperatures of 7000–8000 K, a little higher than the best-fitting hot blackbody temperatures listed in Table 7. This might be attributable to the effects of internal dust extinction on the emergent optical energy distribution in the RT models. The best-fitting models for the different epochs were not homologous, in that the $R_{\rm in}$ and $R_{\rm out}$ values did not increase linearly with time (Table 8). Since the derived dust masses increased by a factor of 4 between days 300 and 464, indicating ongoing dust formation, the dominant dust-emitting regions could change with time.

However, we also investigated homologous models for the different epochs, taking the day 300 value of $Y = 4.0$ from Table 8 and keeping it the same for subsequent epochs, adjusting only the total dust mass to obtain a best fit. These models are plotted as the back solid lines in Fig. 11. They produced slightly improved fits to the day 406 and 464 24-μm data points, although they failed to match the observed SED on day 690 (Fig. 11).

Table 8 shows that the smooth model dust masses increased from 0.4×10^{-4} M$_\odot$ on day 300 to 1.1×10^{-4} M$_\odot$ on day 464 and 4.4×10^{-4} M$_\odot$ on day 690. The inner and outer radii of the day 300 model correspond to expansion velocities of 2700 and 10 800 km s^{-1}, respectively, while those for the day 406 and 464 models correspond to expansion velocities of 2000 and 8000 km s^{-1}, respectively. The above inner radii velocities are consistent with line absorption minimum velocities measured in optical spectra obtained at these epochs, e.g. Sahu et al. (2006) measured Fe II absorption minimum expansion velocities of ∼2000 km s^{-1} after day 150. Since absorption-line optical depths scale as $\int n{\rm d}r$, where n is the density, then for $n \propto r^{-2}$ or steeper density distributions, line optical depths are strongly weighted to the inner radii, where velocities are lowest, as are emission lines, whose emissivities typically scale as $\int 4\pi r^2 n^2 {\rm d}r$. At the earliest epochs, however, when ejecta densities are much higher, line optical depths of unity do not penetrate very deep into the outermost layers of the ejecta, where expansion velocities are much higher, e.g. the day 25 spectrum of Sahu et al. (2006) showed Hα and Hβ absorption minima at expansion velocities of ∼8000 km s^{-1} (their fig. 9), consistent with the outer radius expansion velocities of our dust models, while Hα absorption was even detectable out to −14 500 km s^{-1} on day 25.

7.2 Clumpy dust models

For the Type II SN 2003gd, Sugerman et al. (2006) demonstrated that smooth dust models could underestimate the dust mass by an order of magnitude or more compared to models that allow for clumping. Ercolano et al. (2007) showed that both smooth and clumpy dust models could fit the observed SEDs of SN 1987A at late epochs, with clumpy models able to accommodate significantly larger dust masses. We have constructed clumpy models for SN 2004et, employing a similar modelling strategy to that used for SN 1987A and SN 2003gd.

For the clumpy models, we assume that dense homogeneous clumps are embedded in a less dense ICM with an r^{-2} density distribution. The clumps have radius $\delta \times R_{\rm out}$ and a volume filling factor, f. We adopted the same $\delta = 1/30$ and $f = 0.01$ for all epochs. The density contrast between the clumps and the smooth ICM is defined by $\alpha = N_{\rm clump}(R_{\rm in})/N_{\rm smooth}(R_{\rm in})$, where $N_{\rm clump}(R_{\rm in})$ and $N_{\rm smooth}(R_{\rm in})$ are the densities of the clumps and the smooth ICM at the inner radius, respectively. We set $\alpha = 55$ for all epochs. For the other parameters, we adopted the same source luminosity, temperature, dust composition and size distribution as used for the smooth dust models. Similar SEDs to those from the smooth dust models were obtained for the clumpy models (red dashed curves in Fig. 11). Compared to the variable-Y smooth dust models, the counterpart clumpy models produced an improved fit to the 3.6-μm photometry on days 300–360 and to the 24-μm photometry on days 300–406.

Compared to the smooth dust distribution models, the clumped dust models were able to accommodate two to five times larger dust masses without increasing the effective dust optical depths in the visible region of the spectrum. The smooth and clumpy dust models for day 690 both predict an effective optical depth of 1.3 in the V band, consistent with our estimate from the observed light curve of 0.8–1.5 mag of internal extinction at this epoch (Section 5.2). The clumped dust model for 690 listed in Table 8 had a total dust mass of 1.5×10^{-3} M$_\odot$, but we found that up to 4×10^{-3} M$_\odot$ of dust could be accommodated in clumps at that epoch without seriously reducing the goodness of fit to the observed SED.

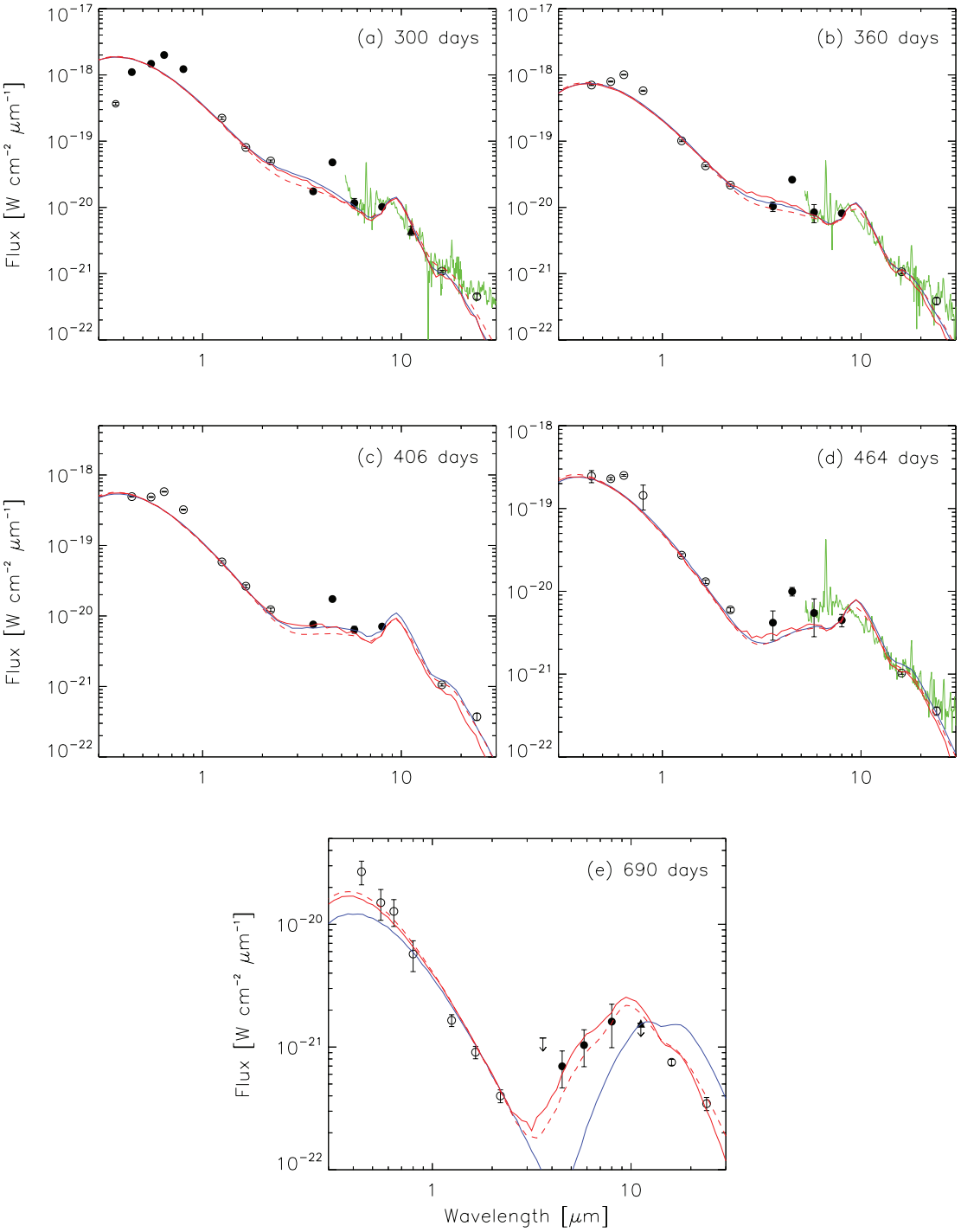

Figure 11. MOCASSIN dust model fits to the optical–IR (0.3–30 μm) SEDs of SN 2004et between days 300 and 690. Filled circles indicate fluxes observed at the epoch of the IRAC observations, whereas open circles indicate optical, NIR and mid-IR photometry which has been interpolated/extrapolated to the epochs of the IRAC observations. The filled triangles indicate the Gemini-Michelle N′-band observations, and upper limits to the flux densities are shown as downward-pointing arrows. *Spitzer* IRS spectra obtained at epochs close to the IRAC observations (on days 294, 348 and 480, respectively: green solid lines) are in good agreement with the mid-IR photometry. Model fits to the data are indicated by the black solid curves (smooth dust distribution, fixed $Y = 4.0$), red solid curves (smooth dust distribution, varying Y) and the red dashed curves (clumpy dust distribution, varying Y). All models adopted a composition of 20:80 per cent amorphous carbon:silicates by mass. See text for further details.

8 DISCUSSION AND CONCLUSIONS

We have used a range of new and archival optical and IR data, extending from day 64 to day 2151, to investigate the formation of dust in the ejecta of the Type II-P SN 2004et, focusing in particular on the mid-IR observations obtained with the *Spitzer Space Telescope* and Gemini-North Telescope.

As discussed by Lucy et al. (1989) for SN 1987A, there are three distinct signatures of dust formation in the ejecta of core-collapse SNe. These are (1) the appearance of asymmetric blueshifted

emission lines caused by dust preferentially extinguishing emission from the receding (redshifted) gas; (2) a drop in visual brightness due to increased extinction by the newly formed dust; accompanied by (3) a mid-IR excess due to thermal dust emission. These three phenomena have all been observed in the case of SN 2004et, as found by previous studies (Sahu et al. 2006; Kotak et al. 2009; Maguire et al. 2010).

From an analysis of new and recalibrated spectra, we showed that between days 259 and 646 the peak of the Hα emission line shifted to the blue by 600 km s^{-1} (Fig. 2). The optical light curve of SN 2004et declined more rapidly than that expected from radioactive deposition, with the onset of ejecta dust formation estimated to have occurred ∼300–400 d after explosion (Fig. 6) The same light curves allowed us to estimate that by day 690 the additional extinction in the V band, attributable to newly formed ejecta dust, was between 0.8 and 1.5 mag. From day 300 onwards, the SN 2004et SEDs exhibit clear excess mid-IR emission relative to blackbodies extrapolated from the optical. The day 300, 360 and 406 SEDs could each be fitted by two blackbody components: (i) a hot component attributed to emission from optically thick gas and (ii) a warm component attributed to dust freshly synthesized and radioactively heated in the SN ejecta (Fig. 8). While these two-component fits provided adequate matches to the observed SEDs out to 16 μm, they did underpredict the 24-μm fluxes, which remained relatively constant between days 315 and 709 (Fig. 4). The day 294, 348 and 480 *Spitzer* IRS spectra (Fig. 11) also confirm the presence of relatively steady excess emission longwards of 20 μm at these epochs. By day 464, a cool third component was definitely required to fit an increasing excess seen in the 16-μm photometry.

For days 300–690, our ejecta dust RT modelling was able to match the observed SEDs out to 20 μm (Fig. 11), longwards of which the relatively invariant excess emission discussed above was present. The observed rise in mid-IR fluxes after 1000 d coincided with a flattening of the optical and NIR light curves at around this time. This, coupled with the fact that the minimum luminosities estimated from blackbody fitting exceeded those expected from radioactive decay from day 690 onwards implies that an additional emission source is required after that date. One possibility, discussed by Kotak et al. (2009), is that this emission source was due to the formation of a cool dense shell of dust as a result of ejecta–CSM interaction. Another, discussed by Sugerman et al. (in preparation), is that this emission was due to a light echo from pre-existing CSM dust.

For days 300, 360 and 406, the 80 per cent silicate, 20 per cent amorphous carbon dust masses derived from our smooth dust models (Table 8) agree with the silicate dust masses derived by Kotak et al. (2009), but our derived dust masses increase faster than their values from day 464 onwards and are a factor of 5 larger by day 690. The clumped dust models of Kotak et al. (2009) had similar masses to their unclumped dust models, while our clumped models have dust masses that are factors of 2–4 larger than for our smooth dust models (Table 8). The dust mass derived from our day 464 clumped model was 5×10^{-4} M$_\odot$, increasing to 1.5×10^{-3} M$_\odot$ by day 690. This mass of newly formed dust is similar to, or larger than, values derived for a number of other recent Type II-P SNe at similar epochs, e.g. SN 1987A (Wooden et al. 1993; Ercolano et al. 2007), SN 2003gd (Sugerman et al. 2006; Meikle et al. 2007), SN 2004dj (Meikle et al. 2011; Szalai et al. 2011), SN2007it (Andrews et al. 2011) and SN2007od (Andrews et al. 2010). But this mass is still a factor of 100 or more smaller than the CCSN ejecta dust masses estimated to be needed to account for the large quantities of dust observed in some high-redshift galaxies (Kozasa et al. 1989; Todini & Ferrara 2001; Nozawa et al. 2003; Bianchi & Schneider 2007; Dwek et al. 2007; Dwek & Cherchneff 2011) and implies that SNe of this type cannot make a major contribution to the dust content of galaxies, unless their dust masses continue to grow at later epochs than have typically been observed at mid-IR wavelengths.

ACKNOWLEDGMENTS

JF and RW acknowledge STFC funding support. MO and MM acknowledge funding support from NASA JWST grant NAG5-12595 and from *HST*/STScI grant GO-11229.01-A. The work of JEA and GCC has been supported by NSF grant AST-0707691 and NASA GSRP grant NNX08AV36H. A portion of the data was obtained at the Gemini Observatory, which is operated by the Association of Universities for Research in Astronomy (AURA) under a cooperative agreement with the NSF on behalf of the Gemini partnership. Some observations were obtained with the NASA/ESA *HST*, which is operated by the Association of Universities for Research in Astronomy, Inc., under a contract with NASA. This work is based in part on observations made with the *Spitzer Space Telescope*, operated by the Jet Propulsion Laboratory, California Institute of Technology under a contract with NASA.

REFERENCES

Andrews J. E. et al., 2010, ApJ, 715, 541
Andrews J. E. et al., 2011, ApJ, 731, A47
Barlow M. J. et al., 2005, ApJ, 627, L113
Benetti S., Cappellaro E., Turatto M., della Valle M., Mazzali P. A., Gouiffes C., 1994, A&A, 285, 147
Bertoldi F., Carilli C. L., Cox P., Fan X., Strauss M. A., Beelen A., Omont A., Zylka R., 2003, A&A, 406, L55
Bianchi S., Schneider R., 2007, MNRAS, 378, 973
Bohlin R. C., 2007, in Sterken C., ed., ASP Conf. Ser. Vol. 364, The Future of Photometric, Spectrophotometric and Polarimetric Standardization. Astron. Soc. Pac., San Francisco, p. 315
Bouchet P., Danziger I. J., 1993, A&A, 273, 451
Branch D., Venkatakrishna K. L., 1986, ApJ, 306, L21
Cardelli J. A., Clayton G. C., Mathis J. S., 1989, ApJ, 345, 245
Danziger I. J., Fosbury R. A. E., Alloin D., Cristiani S., Dachs J., Gouiffes C., Jarvis B., Sahu K. C., 1987, A&A, 177, L13
Dolphin A. E., 2000, PASP, 112, 1397
Dolphin A. E., 2009, PASP, 121, 655
Draine B. T., Lee H. M., 1984, ApJ, 285, 89
Ducati J. R., Bevilacqua C. M., Rembold S. B., Ribeiro D., 2001, ApJ, 558, 309
Dwek E., Cherchneff I., 2011, ApJ, 727, A63
Dwek E., Galliano F., Jones A. P., 2007, ApJ, 662, 927
Ercolano B., Barlow M. J., Storey P. J., Liu X., 2003, MNRAS, 340, 1136
Ercolano B., Barlow M. J., Storey P. J., 2005, MNRAS, 362, 1038
Ercolano B., Barlow M. J., Sugerman B. E. K., 2007, MNRAS, 375, 753
Evans A., 1993, The Dusty Universe. Ellis Horwood, New York
Fabbri J., 2011, PhD thesis, Univ. College London
Fabbri J., Sugerman B., Barlow M., 2005, IAU Circ., 8489, 1
Filippenko A. V., 1997, ARA&A, 35, 309
Filippenko A. V., Foley R. J., Treu T., Malkan M. A., 2004, IAU Circ., 8414, 1
Fitzgerald M. P., 1970, A&A, 4, 234
Fransson C., Grewing M., Cassatella A., Wamsteker W., Panagia N., 1987, A&A, 177, L33
Gerardy C. L. et al., 2002, ApJ, 575, 1007
Glass I. S., 1999, Handbook of Infrared Astronomy. Cambridge Univ. Press, Cambridge

Gordon K. D. et al., 2005, PASP, 117, 503
Hamuy M., Suntzeff N. B., 1990, AJ, 99, 1146
Herrmann K. A., Ciardullo R., Feldmeier J. J., Vinciguerra M., 2008, ApJ, 683, 630
Karachentsev I. D., Sharina M. E., Huchtmeier W. K., 2000, A&A, 362, 544
Kennicutt R. C. et al., 2003, PASP, 115, 928
Kirshner R. P., Oke J. B., Penston M. V., Searle L., 1973, ApJ, 185, 303
Kotak R., Meikle P., van Dyk S. D., Höflich P. A., Mattila S., 2005, ApJ, 628, L123
Kotak R. et al., 2009, ApJ, 704, 306
Kozasa T., Hasegawa H., Nomoto K., 1989, ApJ, 344, 325
Li H., McCray R., Sunyaev R. A., 1993, ApJ, 419, 824
Li W., van Dyk S. D., Filippenko A. V., Cuillandre J.-C., 2005, PASP, 117, 121
Lucy L. B., Danziger I. J., Gouiffes C., Bouchet P., 1989, in Tenorio-Tagle G., Moles M., Melnick J., eds, IAU Colloq. 120: Structure and Dynamics of the Interstellar Medium, Lecture Notes in Physics Vol. 350, Dust Condensation in the Ejecta of SN 1987A. Springer-Verlag, Berlin, p. 164
Maguire K. et al., 2010, MNRAS, 404, 981
Maiolino R., Schneider R., Oliva E., Bianchi S., Ferrara A., Mannucci F., Pedani M., Roca Sogorb M., 2004, Nat, 431, 533
Makovoz D., Roby T., Khan I., Booth H., 2006, in Lewis H., Bridger A., eds, Proc. SPIE Vol. 6274, Advanced Software and Control for Astronomy. SPIE, Bellingham, p. 10
Mathis J. S., Rumpl W., Nordsieck K. H., 1977, ApJ, 217, 425
Meikle W. P. S. et al., 2007, ApJ, 665, 608
Meikle W. P. S. et al., 2011, ApJ, 732, A109
Meixner M. et al., 2010, PASP, 122, 451
Misra K., Pooley D., Chandra P., Bhattacharya D., Ray A. K., Sagar R., Lewin W. H. G., 2007, MNRAS, 381, 280
Nozawa T., Kozasa T., Umeda H., Maeda K., Nomoto K., 2003, ApJ, 598, 785
Nugent P. et al., 2006, ApJ, 645, 841
Panagia N., 2003, in Weiler K., ed., Lecture Notes in Physics Vol. 598, Supernovae and Gamma-Ray Bursters. Springer-Verlag, Berlin, p. 113
Patat F., Barbon R., Cappellaro E., Turatto M., 1994, A&A, 282, 731
Pozzo M. et al., 2006, MNRAS, 368, 1169
Richardson D., Thomas R. C., Casebeer D., Blankenship Z., Ratowt S., Baron E., Branch D., 2001, BAAS, 33, 1428
Sahu D. K., Anupama G. C., Srividya S., Muneer S., 2006, MNRAS, 372, 1315
Schlegel D. J., Finkbeiner D. P., Davis M., 1998, ApJ, 500, 525
Stetson P. B., 1987, PASP, 99, 191
Sugerman B. E. K., Lawrence S. S., Crotts A. P. S., Bouchet P., Heathcote S. R., 2002, ApJ, 572, 209
Sugerman B. E. K., Crotts A. P. S., Kunkel W. E., Heathcote S. R., Lawrence S. S., 2005, ApJS, 159, 60
Sugerman B. E. K. et al., 2006, Sci, 313, 196
Suntzeff N. B., Bouchet P., 1990, AJ, 99, 650
Szalai R., Vinko J., Balog Z., Gaspar A., Block M., Kiss L. L., 2011, A&A, 527, A61
Thatte D. et al., 2009, NICMOS Data Handbook, 8th edn. Space Telescope Science Institute, Baltimore, MD
Todini P., Ferrara A., 2001, MNRAS, 325, 726
Tomaney A. B., Crotts A. P. S., 1996, AJ, 112, 2872
Walker A. R., Suntzeff N. B., 1991, PASP, 103, 958
Welch D. L., Clayton G. C., Campbell A., Barlow M. J., Sugerman B. E. K., Meixner M., Bank S. H. R., 2007, ApJ, 669, 525
Wesson R. et al., 2010, MNRAS, 403, 474
Wooden D. H., Rank D. M., Bregman J. D., Witteborn F. C., Tielens A. G. G. M., Cohen M., Pinto P. A., Axelrod T. S., 1993, ApJS, 88, 477
Woosley S. E., Hartmann D., Pinto P. A., 1989, ApJ, 346, 395
Zubko V. G., Mennella V., Colangeli L., Bussoletti E., 1996, MNRAS, 282, 1321
Zwitter T., Munari U., Moretti S., 2004, IAU Circ., 8413, 1

APPENDIX A: PHOTOMETRIC DATA PROCESSING

A1 Mid-IR data processing

The earliest *Spitzer* data for the field around SN 2004et were obtained by the SINGS Legacy team (Kennicutt et al. 2003), who produced enhanced data products which could be downloaded from the SINGS Legacy Data Deliveries section[4] of the Spitzer Science Center (SSC) website. The MIPS 24-μm mosaic of NGC 6946 (providing a pre-explosion image of the field around SN 2004et at day −75) were downloaded from the SINGS fifth and final data delivery. The mosaic was created from multiple *Spitzer* images obtained in scan-mapping mode over 2 d (75 and 73 d prior to the explosion of SN 2004et) and processed with the MIPS data analysis tool version 3.06 (Gordon et al. 2005), along with additional custom processing by the SINGS team.

However, the enhanced SINGS IRAC data were not used, due to the unusually long time-span between the two observations of NGC 6946 (∼6 months, compared to the usual 1 or 2 d) which were combined by the SINGS team to construct the final enhanced mosaic. Instead, the standard basic calibrated data (BCD) pipeline data for each day (corresponding to the pre-explosion image at day −104 and the first mid-IR post-explosion image at day 64) were downloaded from the *Spitzer* archive and processed along with the rest of the *Spitzer* observations as described below.

The BCD from the *Spitzer* pipeline were combined into final mosaic images using the *Spitzer* MOPEX software package (Makovoz et al. 2006), which includes outlying-pixel rejection, background matching and mosaicking with drizzling to increase the sampling of the PSF. The IRAC and MIPS data were redrizzled to plate scales of 0.75 and 1.5 arcsec pixel^{-1}, respectively (compared to the standard *Spitzer* pipeline products with a spatial sampling of 1.2 arcsec pixel^{-1} for IRAC and 2.45 arcsec pixel^{-1} for MIPS), following the pixel sizes adopted by the SINGS team for producing their enhanced data products. The PUI data were redrizzled to a plate scale of 1.2 arcsec pixel^{-1} (compared to the standard pipeline data with a spatial sampling of 1.8 arcsec pixel^{-1}). The final mosaic images for all three *Spitzer* instruments were calibrated in surface brightness units of MJy sr^{-1} during the BCD pipeline stage.

For the IRAC and MIPS 24-μm data, PSF-matched difference images, which used the pre-explosion SINGS mosaics as the reference images, were produced as follows. The final mosaics produced by MOPEX were geometrically registered to a common reference frame using matching point sources identified within the fields of view, with a second-order general fit within the IRAF `geotran` task. In all cases, registration residuals were less than 0.1 pixel rms in both the x and y dimensions. Once registered, the data were PSF-matched and differenced using the DIFIMPHOT package (Tomaney & Crotts 1996) as implemented and modified by Sugerman et al. (2005). Two approaches were taken to PSF matching. In the first, an empirical PSF was built for each image using uncrowded point sources combined using the DAOPHOT PSF-building tasks (Stetson 1987). In the second, these same tasks were run on a single theoretical PSF available for each *Spitzer* IRAC and MIPS 24-μm image from the archive after that model had been rotated and scaled according to the data's particular plate scale and position angle. Images were PSF-matched separately using the empirical and theoretical PSFs, photometrically scaled by the median brightness of a number

[4] http://ssc.spitzer.caltech.edu/legacy/singshistory.html

of matching point sources, and then subtracted to yield the final difference images. In general, the difference images made using the theoretical PSFs were of higher quality (i.e. smaller subtraction residuals and less background noise) since the shapes of *Spitzer*'s PSFs have varied little during its mission. In practice, these techniques allow the reliable detection and measurement of changes in point sources that would be considered below the 1σ level in direct, undifferenced images (Sugerman et al. 2002).

For the photometry from the IRAC and MIPS difference images, uncertainties were measured with a custom implementation of an optimal photometry code written for the original version of DIFIMPHOT, which includes the full noise model of the DAOPHOT `allstar` routine as well as correct noise contributions from both input and reference images and the original sky values in each image prior to pipeline calibration.

The Gemini-Michelle data were downloaded from the Gemini Science Archive and processed with the Gemini IRAF `midir` tasks and further cleaning procedures. The fluxes, or upper limits, in counts measured from the final average-combined images were converted to F_ν flux density units by multiplying by flux conversion factors derived from aperture photometry of standard stars.

A2 Optical and NIR data processing

Gemini/GMOS-N. On days 317, 404 and 664, 60-s images were taken with GMOS-N in the g', r' and i' broad-band filters. Longer exposures of 2×600 s in the same filters were taken at day 1412 when the SN was expected to have faded. The images were reduced using the Gemini IRAF package. Pipeline-processed bias and flat-field images were obtained from the Gemini Science Archive. Object images were trimmed, corrected for overscan and bias, and flat-fielded using the `gsreduce` task. Finally, `gmosaic` was used to mosaic the three GMOS CCDs into a single image. PSF-fitted photometry was performed on the SN and a sample of standard stars from the photometric V, R and I sequence of Pozzo et al. (2006) to establish the nightly zero-point. The GMOS Sloan Digital Sky Survey (SDSS) magnitudes were transformed into Johnson V, R and I magnitudes using the transformation equations given by Welch et al. (2007). These linear transformations were derived from the photometric V, R and I sequence presented by Pozzo et al. (2006).

Gemini/NIRI. In order to ensure a consistent sky background between exposures, individual exposures of 30 s in each of the broad-band *JHK* filters were taken, with the total number being dictated by the anticipated decline of the SN NIR light. A 5-arcsec dither pattern was employed to ensure efficient removal of point sources while making sky images. Data reduction for each night was performed using the standard NIRI routines within the Gemini IRAF package. `nprepare` and `niflat` were used to derive the normalized flat-field and the bad pixel mask, while `nisky` was used to create the final sky image. `nireduce` was used to subtract this sky image from and apply the flat-field correction to the processed object images. Finally, the individual images in each filter were co-added using the GEMTOOLS routine `imcoadd`. PSF-fitted photometry was performed on SN 2004et and three standard stars present within the field. The *JHK* magnitudes of the standard stars are contained within the Two Micron All Sky Survey (2MASS) catalogue and were used to derive the nightly zero-point in each filter. The photometric uncertainty is dominated by the standard deviation of the zero-point derived from the three standard stars.

Tenagra and Steward/Bok. These early optical and NIR data were reduced, calibrated and measured in a similar manner to the GMOS-N and NIRI observations described above, using standard routines within IRAF. The data were bias and dark subtracted, flat-fielded, and the multiple exposures were combined to form the final image.

HST *WFPC2 and NICMOS2*. For the WFPC2 observations, imaging with the broad-band *F606W* and *F814W* filters was used to measure the V- and I-band flux densities. For the NICMOS2 observations, imaging was carried out with the *F110W*, *F160W* and *F205W* filters, most closely representing the standard *JHK* bands. Small-scale dithering was employed for both instruments to improve S/N, remove cosmic rays and to improve the pixel scale of the final images by drizzle techniques. The WFPC2 observations used a four-point dither $\times 400$ s exposure for each band. The NICMOS2 observations used a five-point dither $\times 128$ s in the *F110W* and *F205W* filters and a four-point dither $\times 128$ s for *F160W*.

The data were reduced and calibrated using the IRAF external package `stsdas` (version 3.8) and included the removal of cosmic rays and other artefacts, as well as linearity corrections. High-resolution images were created using the `stsdas/drizzle` package, and additional distortion correction and alignment was performed using background stars. The PSF of these reference background stars were fitted by Gaussian profiles to obtain accurate positions, and then instrumental distortions were corrected with the IRAF tasks `xyxymatch`, `geomap` and `geotran`. The resultant pixel scale is $\sim$0.02 arcsec pixel^{-1} in the WFPC2 images and $\sim$0.04 arcsec pixel^{-1} in the NICMOS2 images. The FWHM of the PSFs was $\sim$3 pixel. Flux measurements were performed using the IRAF DAOPHOT tasks. For the WFPC2 data, *HST* magnitudes were converted to the Johnson–Cousins system using the transforms of Dolphin (2000, 2009), which include charge transfer efficiency (CTE) corrections.

Whilst the broad-band NICMOS filters, *F110W*, *F160W* and *F205W*, are roughly equivalent to the J, H and K filters, respectively, colour transformations are not well constrained for late-time SN spectra at NIR wavelengths, and consequently magnitudes were not converted to the standard *JHK* photometric system. The late-time *HST*-NICMOS magnitudes listed in Table 6 are for the *HST* filters in the Vegamag system, which uses an estimate of the flux density of Vega, from synthetic spectra integrated over the NICMOS bandpasses, as a photometric zero-point. For each filter and epoch, the measured count rate (CR; in units of DN s^{-1}) at the position of the SN was converted to flux by multiplication with the PHOTFNU (Jy s DN^{-1}) conversion factor given in the fits header, where PHOTFNU is the bandpass-averaged flux density for a source that would produce a CR of 1 DN^{-1}. An approximate Vega-normalized magnitude was then calculated from the following equation (NICMOS data handbook; Thatte, Dahlen & others 2009):

$$m = \mathrm{ZP(Vega)} - 2.5 \log_{10}(\mathrm{PHOTFNU} \times \mathrm{CR} \times \langle F_\nu(\mathrm{Vega}) \rangle^{-1}),$$

where $\langle F_\nu(\mathrm{Vega}) \rangle$ is the bandpass-averaged flux density (in Jy) for the NICMOS filters using a model reference spectrum of Vega[5] (Bohlin 2007) and ZP(Vega) is the magnitude of Vega, which is defined to be 0.00 mag under the California Institute of Technology (CIT) infrared photometry scale.

WIYN/WHIRC. The WHIRC (Meixner et al. 2010) has a 2048×2048 HgCdTe VIRGO detector with a pixel scale of $\sim$0.1 arcsec pixel^{-1}. Sky conditions during the observation were fair, with a seeing of $\sim$0.8 arcsec. To minimize the effects of high background levels and pixel-to-pixel variations on the array,

[5] Taken from the NIC2 table of Photometric Keywords and Vegamag Zeropoints at http://www.stsci.edu/hst/nicmos/performance/photometry/postncs_keywords.html

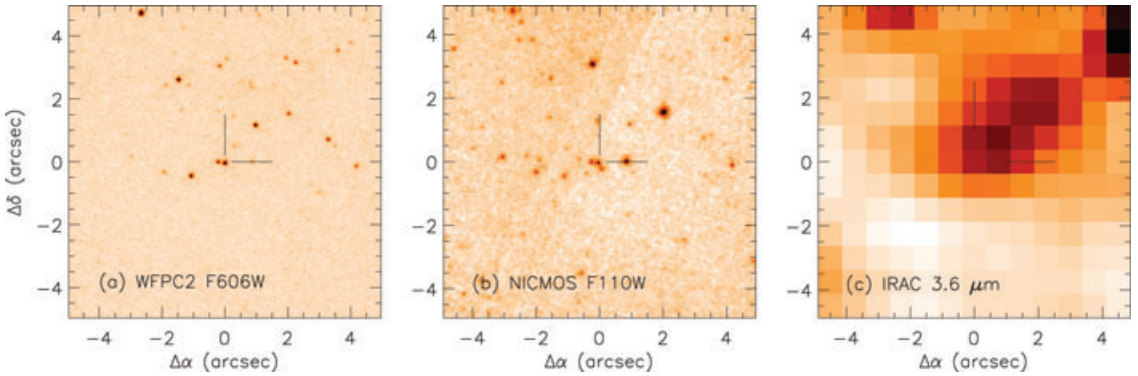

Figure A1. Late-time high-resolution *HST* images reveal a complex field compared with *Spitzer* IRAC data. Panel (a) shows the WFPC2 *F606W* image at day 1019 with a 5×5 arcsec^2 FoV centred on the SN position. A source assumed to be the SN is located at the centre of the image (indicated by the cross-hairs), with a close companion to the east ('star 2') which is detected in both WFPC2 filters. Panel (b) shows the equivalent field in the NICMOS *F110W* filter at the same epoch. Star 2 is detected in all the three NICMOS filters together with an additional red object just south of the SN position. For comparison, panel (c) shows the *Spitzer* IRAC 3.6-μm image at day 1054.

dithering techniques were employed, whereby the source was offset in each frame of a series of exposures. The offset images were used for sky level corrections. Data reduction was carried out using standard IRAF tasks. The array linearity correction was performed using the WHIRC task `wprep`, and a distortion correction was applied using files downloaded from the WIYN-WHIRC web page.[6] A selection of 2MASS stars close to SN 2004et was used for final flux calibration, and flux measurements were performed using the IRAF DAOPHOT package.

The WIYN *H*-band observation of SN 2004et on day 1803 was the last of our NIR observations of the SN, some 5 years after explosion. The SN was not clearly detected due to the contribution from neighbouring stars that were resolved in the high-resolution *HST*-NICMOS observations (on days 1019 and 1215; see the following section). Consequently, an upper limit to the magnitude was derived. The magnitude in an aperture of radius 0.6 arcsec (∼17 pc, for the adopted distance of 5.9 Mpc) was measured using the IRAF DAOPHOT tasks. Estimated contributions from three neighbouring stars resolved in the high-resolution NICMOS *F160W* filter ($\simeq H$ band) were measured from the NICMOS data and subtracted from the WIYN magnitude to provide the final upper limit presented in Table 6.

A3 Late-time high-resolution *HST* images

The late-time high-resolution *HST* images reveal that the single point source seen at the SN position in the *Spitzer* images is actually a complex field comprised of at least three sources. Fig. A1 shows example *HST* WFPC2 *F606W* ($\approx V$) and NICMOS *F110W* ($\approx J$) images from 2007 July (day 1019) compared to the *Spitzer* IRAC 3.6-μm image from 2007 August (day 1054). Each field of view is centred on the position of the SN and a source is located at this position, indicated by the cross-hairs. The star to the east ('star 2') was detected in both WFPC2 filters and all three NICMOS filters at days 1019 and 1215. The third star to the south of the SN position ('star 3') was detected in all three NICMOS bands but was not detected in the WFPC2 filters at either epoch.

The magnitude of star 2 was measured from the WFPC2 images and transformed to V- and I_c-band magnitudes as described previously for the SN.

The V and I_c magnitudes of star 2 were dereddened using $E(B-V) = 0.41$ mag (Zwitter et al. 2004) and adopting the extinction law of Cardelli et al. (1989) with $R_V = 3.1$, corresponding to $A_V = 1.27 \pm 0.22$ mag. The intrinsic $(V-I)_c$ colour was then used to estimate an R_c-band magnitude using a table of intrinsic colours as a function of spectral type compiled by the Space Telescope Science Institute (STScI)[7] based on the work of Fitzgerald (1970) and Ducati et al. (2001). The derived colour index of $(V-I)_c = 0.8$ indicated star 2 was probably a K1.0 star with an intrinsic R_c magnitude of ∼22.5. The equivalent reddened R_c magnitude of 23.53 ± 0.50 was in reasonable agreement (within the errors) with a magnitude estimated from fitting two PSFs to the blended 'SN plus star 2' in the R_c-band GMOS-N image at day 1412. This PSF-fitted measurement gave an R_c-band magnitude for star 2 of 23.63 ± 0.19. A *B*-band magnitude for star 2 of 25.46 ± 0.50 was estimated in the same way.

The estimated reddened B and R_c magnitudes of star 2, together with the measured V and I_c magnitudes, were subtracted from the optical magnitudes of SN 2004et obtained from the Subaru-FOCAS and GMOS-N observations from day 646 onwards. During this time, the SN had faded substantially such that the neighbouring star 2 made a significant contribution to the brightness measured at those epochs. At day 646, the estimated contribution from star 2 was ∼8 per cent in the V band and ∼10 per cent in the I_c band, whilst by day 1412, the contribution was almost half that of the total flux in both bands. For epochs earlier than day 500, the brightness contribution from star 2 was ≤1 per cent.

The late-time Gemini-NIRI photometry at day 652 has not been corrected for contamination by stars 2 and 3. As previously explained, the NICMOS magnitudes are listed in the *HST* Vegamag system, and were not converted to the standard *JHK* photometric system since colour transformations are not well constrained for late-time SN spectra at NIR wavelengths. It is possible that these neighbouring stars made a small but significant (∼10 per cent) contribution to the brightness measured in the NIRI observations at day 652, so the uncertainties on the day 690 interpolated flux densities in Table 6 have been increased to reflect this by adding a further 10 per cent error in quadrature to the original flux uncertainty.

[6] http://www.noao.edu/wiyn/

[7] http://www.stsci.edu/inr/intrins.html

This paper has been typeset from a TEX/LATEX file prepared by the author.